UNIVERSITY
OF OSLO

Master's thesis

Tailoring functional properties of earth-abundant II-IV-nitride alloys: towards tandem solar cell applications

Dina Marie Nielsen

Material Science and Nanotechnology
60 ECTS study points

Department of Chemistry
Faculty of Mathematics and Natural Sciences

Spring 2023

Dina Marie Nielsen

Tailoring functional properties of earth-abundant II-IV-nitride alloys: towards tandem solar cell applications

Supervisors:
Vegard Skiftestad Olsen
Lasse Vines

Abstract

Zn-IV-nitrides are a promising group of novel semiconductors, exhibiting similar optoelectrical properties, as well as property tunability, as the group of III-nitrides. Compared to the III-nitrides, the Zn-IV-nitrides have shown to be earth abundant, non-toxic and less expensive candidates. $ZnSnN_2$ and $ZnGeN_2$ are two ternary semiconductors, each possessing properties suitable for solar absorbers. $ZnSnN_2$ have been shown to have an optimal bandgap size for a top cell in a tandem solar cell with Si bottom cell, whereas the electrical properties are unfavorable. $ZnGeN_2$ on the other hand, has a higher bandgap, but also a lower and more fitting carrier concentration for use in tandem solar cells. Based on this an alloy of the two materials were grown and investigated with respect to the structural, optical and electrical properties of the material.

In this work stoichiometric and non-stoichiometric $ZnSn_xGe_{1-x}N_2$ alloys were grown with reactive RF with HiPIMS co-sputtering, with the aim of gaining a better understanding and control of the optoelectrical properties. The stoichiometric alloy was continuous, without phase segregation and yielded high crystal quality. The alloy also exhibited a tunable bandgap similar to the InGaN alloy, as well as tunable carrier concentration as a function of alloy composition. The research resulted in a bandgap in a the range of 1.56 eV to 3.04 eV, and a carrier concentration from 7.38×10^{20} cm^{-3} - 1.51×10^{18} cm^{-3} from $ZnSnN_2$ to $ZnGeN_2$, i.e., the end-point materials, respectively. Both functional properties in addition to the c-lattice parameter were tunable with an almost linear behavior as a function of the alloy composition. Importantly, the measured mobility for the $ZnGeN_2$-rich compositions was significantly higher than all reported values.

A non-stoichiometric $ZnSn_xGe_{1-x}N_2$ alloy were also grown to investigate if the carrier concentration could be reduced even more than for the stoichiometric alloy, based on similar successful approach for $ZnSnN_2$. This was to some extend achieved, but not in the extend we aimed for. This is likely due to not sufficient non-stoichiometry of the thin films. The crystal quality decreased for the non-stoichiometric alloy series. The alloys showed a similar tunability of the bandgap, but with slightly lower bandgap energies than their stoichiometric equivalent alloy composition. The the carrier concentration of the non-stoichiometric alloys were tunable from 3.51×10^{20} cm^{-3} - 5.96×10^{16} cm^{-3}.

Acknowledgements

I would like to express my deepest gratitude to my supervisor, Dr. Vegard Skiftestad Olsen, for all your support and guidance, and for allowing me to take part in your project on II-IV nitrides. I would like to thank you for always keeping your door open and for making my days better with early morning coffees, fun jokes and a big smile. I could not have asked for a better supervisor. I would also like to extend my sincere thanks to my co-supervisor, Prof. Lasse Vines, for your insightful advice, valuable feedback, and dedicated time and effort in proofreading my thesis.

I would like to thank the LENS group, and the people participating in the solar meetings for fine discussions. Thanks to Dr. Eirini G. Zacharaki for her contributions in conducting FTIR measurements, Kjetil Karlsen Saxegaard for teaching and assisting me on the SEM, Vegard Rønning for teaching me the laser cutter, Dr. Simon Cooil for conducting XPS and UPS measurements on our samples and Viktor Bobal for ion-implantations.

Finally, I would like to express my appreciation to my fellow MENA students, especially Lars Kristian and Daniil for making these two years a fun and memorable experience. I would also like to thank my friends and family for their support, encouragement, and love, especially my mom and Sondre.

Contents

Chapter 1

Introduction

As the world's population increases and the living conditions in many parts of the world is improving, the global energy consumption grows at an increasingly rapid rate. One of the main challenges facing humanity is to provide the world with energy in a way that is environmentally sustainable and climate friendly. However, a large portion of this demand is currently met by fossil fuels, which have negative effects on the environment. It is therefore crucial to transition towards renewable energy sources, solar energy being one of them.

Today's solar industry is primarily dominated by silicon-based solar cells. Silicon is an earth-abundant element with an established industry, making it a relatively low-cost option for solar cell production. However, conventional silicon solar cells are not very efficient with a theoretical upper limit of less than about 30% efficiency [1]. One approach to improve today's solar cells is to harvest energy from a larger part of the solar spectrum by the use of tandem solar cells. A tandem solar cell (TSC) consists of different solar cells on top of each other, where each solar cell has the task of converting different parts of the solar spectrum to electricity. TSC's can be constructed by many different material systems, but one very intriguing approach is to place a second solar cell on top of the well-known Si-cell. The transparent top cell will absorb the photons with higher energies, whereas the lower energy photons are transmitted to the Si-cell. The TSC have some requirements that must be met before they can be commercially attractive, such as their electrical and optical properties must be compatible to the Si bottom cell. In addition, they must be reasonably inexpensive and suitable for large-scale production. The materials used in the manufacturing of the TSC's should ideally be earth abundant, non-toxic and easy to extract.

III-nitrides, such as AlN, GaN and InN, are today one of the most important semiconductor families within optoelectronics. They are, together with their alloys, the cornerstone in blue-, and hence also white LED technology, and are also employed in high-quality solar cells. On the other hand, these materials are expensive, not earth-abundant and they require growth techniques such as metalorganic chemical vapor deposition (MOCVD) or molecular beam epitaxy (MBE), methods that are not suitable for large scale production. As an alternative, II-IV-nitrides have been found to possess similar optoelectronic properties as III-nitrides, and has recently gained attention. For the II-IV-nitrides, the III-element (in

III-nitrides) is substituted with 50% II-elements and 50% IV-elements. The advantages of the II-IV-nitrides are that they potentially could be more cost-efficient and more suitable for industrial scaling. In addition, II-IV-nitrides, such as Zn-IV-N_2, with IV = Sn, Ge or Si, are composed of earth-abundant and non-toxic elements. The bandgap (E_g) of the Zn-IV-N_2's are very similar to the mentioned III-nitrides, so their alloys should have E_g tunable from UV to IR part of the spectrum. This makes the Zn-IV-N_2 family a strong candidate for a top cell in a Si-based TSC.

$ZnSnN_2$ and $ZnGeN_2$ are two novel earth-abundant semiconducting materials that possess different suitable qualities as a top layer in a tandem solar cell. $ZnSnN_2$ has indeed been found to have E_g close to 1.7 eV [2], which has been calculated to be the optimal bandgap energy for a top cell material in a two-terminal solar cell together with Si [3]. The main challenge to overcome for $ZnSnN_2$, is the unintentionally high carrier concentration (n), making it unsuitable for pn-junctions and thus also solar cells. $ZnGeN_2$ is known to have a much lower carrier density than $ZnSnN_2$, but has also a much wider bandgap, of approximately 3.1 eV [4]. Fabrication of an alloy between these two semiconductors makes it possible to achive a tunable carrier concentration and bandgap, by changing the compositional ratios [4, 5, 6]. The carrier mobility on the other hand, still remains unfavorably low, i.e., < 20 cm^2Vs [6]. For $ZnSn_xGe_{1-x}N_2$ to be working as a top cell in a tandem solar cell with an Si bottom cell, the material should have an $E_g \approx 1.7$ eV, have as high carrier mobility as possible, and have a carrier concentration in the range of $10^{16} - 10^{17}$ cm^3, in order to be current-matched with the Si bottom cell, increase the carrier lifetime, and be compatible for pn-junctions, respectively.

A method found to reduce n in $ZnSnN_2$ is non-stoichiometric growth [7]. In addition to several dominating intrinsic donor defects, such as the Sn_{Zn} antisite, the Zn_{Sn} antisite is a double acceptor. By growing Zn-rich $ZnSnN_2$ the formation probability of these acceptor defects will increase and thus lower the number of carriers. As Ge, just as Sn, is a four-valente element, Zn_{Ge} antisites would in theory also act as double acceptors. The growth of non-stoichiometric Zn-rich $ZnSn_xGe_{1-x}N_2$ is therefore fabricated as an attempt to reduce the high carrier concentration. $ZnSn_xGe_{1-x}N_2$ was grown by magnetron sputtering, which is a method based on the bombardment of a target material by plasma ions, sputtering off target atoms in the direction of a substrate. The sputtering process was reactive, which means that nitrogen gas is introduced to react with the sputtered metal atoms. To increase the ionization of nitrogen, we used high-power impulse magnetron sputtering (HiPIMS).

In this master thesis, the structural, optical and electrical properties of a stoichiometric and non-stoichiometric $ZnSn_xGe_{1-x}N_2$ alloy were investigated. The aim of growing $ZnSn_xGe_{1-x}N_2$ alloys was to obtain a tunable bandgap and carrier concentration, as well as to explore if non-stoichiometric growth further reduced the carrier concentration throughout the alloy. This in order to potentially produce an absorbing material well suited for application in a silicon based tandem solar cell. The thesis consists of five chapters. Chapter 2 is an introduction to semiconductor physics, and presents theory and background about the

alloy materials. The experimental methods used in this work is introduced in Chapter 3. Chapter 4 presents the experimental results and discussion, and a conclusion, as well as suggestions for future work is presented in Chapter 5.

Chapter 2

Theory and Background

In this chapter semiconductor theory will be presented, where the aim is to explain some core concepts behind the work of this thesis. First, a description of crystal structures in solid materials and how atoms arrange themselves. Further, the chapter goes into semiconductor physics, describing phenomena that are decisive for material specific properties, and are essential for understanding the behavior of the materials studied in this thesis. This is followed by a section of thin films and different growth modes. The materials studied in this master thesis are introduced in section 2.4 - II-IV-N's, where $ZnSnN_2$, $ZnGeN_2$ and their alloy $ZnSn_{1-x}Ge_xN_2$ are discussed. Lastly, the construction of a pn-junction is presented for a further description of the working principles of a solar cell and also tandem solar cells, as these are applications where the II-IV-N_2 may have significant impact. This chapter is based on the text books Kittel [8], Tilley [9], Nelson [10], Streetman [11], and lays the foundation for further results and discussions in later chapters.

2.1 Crystal Structures

Solid materials can be divided into crystals and non-crystals. Atoms in a solid are closely packed and arrange themselves to minimize their free energy, forming a stable system. If the atoms arrange in a periodic lattice with a particular repeating pattern they form a crystalline solid. Oppositely, amorphous materials are solids without any long-range repeating arrangement of atoms. In a solid, atoms are bound together and their placement relative to each other determines the crystal structure, as well as the electrical and optical properties of the material.

Chemical bonds between the atoms are formed due to strong attractive forces, giving the atoms fixed positions relative to each other. There are three groups that are used when categorizing chemical bonds; covalent-, ionic- and metallic bonds. Covalent bonds are formed between two atoms sharing electrons, and are often the case between identical atoms or atoms with only small differences in electronegativity. Instead of sharing electrons, some atoms become more stable by losing or gaining an entire electron. By losing or gaining an electron, atoms turn into charged particles called ions, where ions with opposite charge attract each other, and by that form ionic bonds. Metallic bonds differ from covalent

and ionic bonds as the electrons in metallic bonds are delocalized, meaning they are not only shared between two atoms, as for covalent and ionic. Instead atoms in metal bonds contribute their valence electrons to a big, shared cloud of electrons. The type of chemical bonds present in a solid determines many of the material properties, such as the electron cloud making metal conductive, or that ionic and covalent bonds co-exists in many semiconductor materials, as in for example gallium nitride (GaN) [12]. Bonds also determine how the atoms arrange themselves, hence the crystal structure.

A crystal lattice is a mathematical description of a crystal structure. A lattice is an infinite pattern of points, where each point must have the same surroundings in the same orientation and each point in the lattice can represent one or several atoms. The periodicity of the lattice can be expressed by primitive vectors **a**, **b** and **c**. These vectors describe a lattice of infinite lattice point, where each point can be expressed by a sum of the primitive vectors

$$\mathbf{R} = u\mathbf{a} + v\mathbf{b} + w\mathbf{c} \tag{2.1}$$

where u, v and w are integers and $\mathbf{R}$ is the translation vector of the lattice. The three vectors span a volume called the unit cell. All three-dimensional lattices can be described by seven different unit cell types, depending on their length and the angles between them. These seven unit cell types give rise to 14 lattices, called Bravais lattices. All crystal structures can be built up from the Bravais lattices by placing an atom or a group of atoms at each lattice point. An easy and well known unit cell is the cubic crystal, which have equal side lengths $a = b = c$ and all angles 90°. Silicon (Si) is a an example of a material with face centered cubic (fcc) crystal structure as shown in figure 2.1c. Three Bravais lattices with cubic unit cells are shown in figure 2.1.

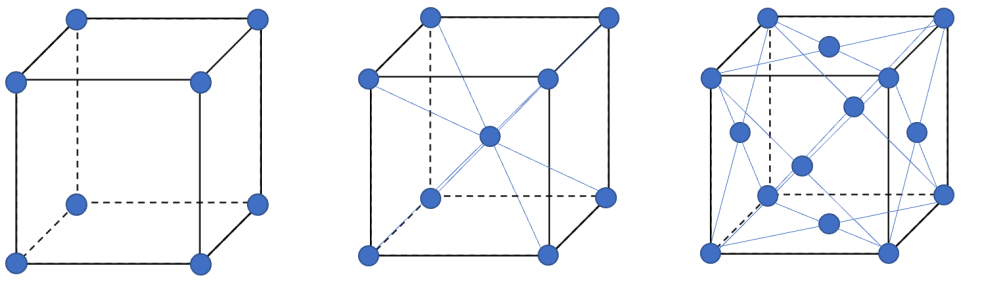

(a) Simple Cubic (b) Body Centered Cubic (c) Face Centered Cubic

Figure 2.1: Three examples of Bravais lattices with cubic unit cells.

Different characterization techniques are used for analyzing materials, and for techniques based on diffraction and scattering processes, the crystal planes are exceptionally important. The orientation of a crystal plane is often described by Miller Indices, where the indices h, k and l represent not only one plane, but a set of parallel planes, *(hkl)*. The indices are defined by how the plane intersects the crystallographic axes of the solid. More precisely, they describe the reciprocal of points where the plane intercepts the primitive vectors. A plane that lies parallel to a primitive vector, and hence never intercepts it, is therefor given

the index 0. Imagining fcc structured silicon, where a plane intercepts vector **a** and **c** equally, but is parallel to vector **b**. Then the reciprocal of the intercepts can be expressed as (1/1, 1/∞, 1/1), giving this particular plain and all parallel planes Miller indices (101) as illustrated in figure 2.2. Correspondingly would the (100) plane intercept vector **a**, but be parallel to vector **b** and **c**. This nomenclature is used for all crystal structures, except for hexagonal crystal structures. Hexagonal crystal structures have a six-fold symmetry, where a 4-index notation *(hkil)* is required for better describing the planes. This is called the Miller-Bravais notation, and for a perfect hexagonal system, one has to make sure that the notation satisfy the relation

$$i = -(h + k) \tag{2.2}$$

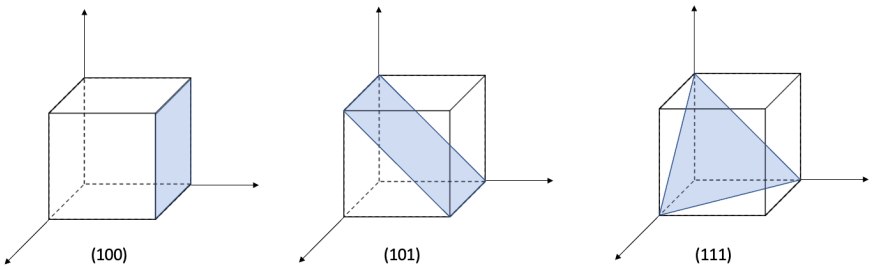

Figure 2.2: Examples of planes with different Miller indices in cubic crystals.

A set of lattice planes (*hkl*) is often represented by a vector, where the length of the vector is inverse of the distance between the lattice planes, and the direction is perpendicular to the (*hkl*) lattice planes. The vector is called the reciprocal lattice vector ($\mathbf{g}_{hkl}$), and the end point of the vector is called the reciprocal lattice point (*hkl*). Variations in the lattice constants and/or the direction of the lattice planes will decide the length and direction of the vector, $\mathbf{g}_{hkl}$. This is especially important for XRD (x-ray diffraction) measurements, where information about the crystal structure is obtained based on the diffraction of lattice planes.

The crystal structure of a solid is of great importance to many chemical and physical properties. Knowledge about and control over the crystallography is essential when developing semiconductor materials used for solar technology, where electrical and optical properties are of major interest.

2.2 Semiconductors

Materials can be classified as metals, insulators and semiconductors based on the position of their energy bands and thus their electrical conductivity. Metals are known to have a high electrical conductivity, due to metal bonds creating free electrons. Insulators on the other hand, have no free electrons and are therefore non-conducting materials, while materials classified as semiconducting have properties in between metals and insulator, which permits them to be used in essential technologies, such as transistors and solar cells.

It is often distinguished between elemental semiconductors (ESC) and compound semiconductors (CSC). ESC contains only one species of atoms, such as silicon (Si) and germanium (Ge), while CSC consists of two or more elements. Gallium nitride (GaN) and zinc oxide (ZnO) are examples of binary compounds, consisting of two different elements. Ternary compounds such as $ZnSnN_2$ and $ZnGeN_2$ are formed with elements from three different columns i.e, II-IV-V's. Pure silicon is the most important semiconducting material for integrated circuit applications, while binary and ternary III-V semiconductors are the cornerstones for light emission applications, such as light emitting diodes (LED).

The most well-known semiconductors are crystalline solids, with Si, Ge and GaN as some recognized examples. Historically, the first decade of semiconductor electronics was entirely based on Ge, and in the last decades there have been renewed interest in Ge, for instance SiGe alloys with the purpose of increasing the channel mobility of Si-based transistors [13]. Si is the dominating semiconductor material used in e.g. photovoltaic technology in solar cells, holding more than 95% share of the photovoltaic market [14]. In recent years the III-V's have had a big impact on especially the optoelectronic industry, where in 2014 Shuji Nakamura, Isamu Akasaki and Hiroshi Amano was awarded the Nobel Prize in Physics for their discovery of GaN-based materials and devices, which led to blue and white LED's [15]. Also amorphous semiconductors can have desired properties. Yan Ye et al. showed in his research on ZnON that highly ordered crystalline structure is not required to achieve a high mobility of the film [16], as previously thought. Amorphous ZnON are today a highly relevant material in display technology.

2.2.1 Electron Energies and Band Structure

Electrons on a single isolated atom have discrete energy states. Each energy state can only be occupied by one electron, and it is therefore impossible for two electrons to occupy the same state. According to Pauli's exclusion principle, when two identical atoms are brought closer together, the energy of their states are split and slightly shifted. In crystals, where the number of atoms can be in the range of 10^{23} cm^{-3}, none of the states are allowed to overlap. Instead the discrete energy states for all the atoms are spread out forming a continuous band. Energies within a band are allowed energy states that electrons can occupy, while gaps between energy bands are forbidden states that electrons are not allowed to occupy, called bandgaps (E_g). The bands and bandgap construct the electronic band structure of different materials, where variations in band structure vary with the elements in a material and the crystal structure.

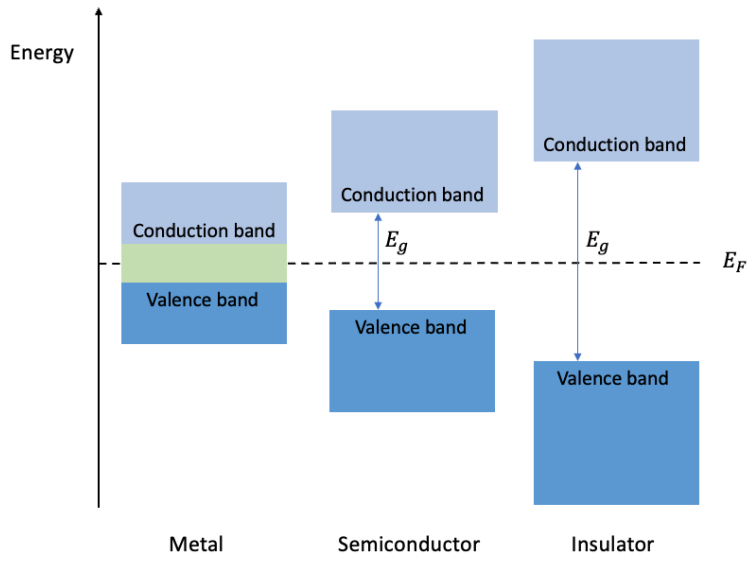

Figure 2.3: Illustration of the difference in bandgap energy for metals, semiconductors and insulators at 0K. Semiconductors and insulators differ mainly in size of their bandgap, whereas metals can have overlapping valence and conduction bands or have a partially filled conduction band.

Figure 2.3 shows the bandgaps for different material groups at 0 K. The highest energy band occupied by electrons at absolute zero is called the valence band (VB), whereas the lowest unoccupied energy band is called the conduction band (CB). The lowest energy in the conduction band is typically referred to as E_c, and highest energy in the valence band, E_v. The energy difference between E_c and E_v is what constitutes the size of E_g.

The size of E_g differentiates metals, semiconductors and insulators and their ability to be conductive. Charge carriers, described more in detail in the subsection below, is a necessity for conductivity and includes free electrons in the CB or holes in the VB. Metals have a partially filled CB or overlapping conduction and valence bands, effectively resulting in no bandgap. This means that they do not require excitation of electrons, i.e., additional energy, to be conductive. Both semiconductors and insulators have a filled VB, and an empty CB at 0 K, making them non-conductive at this temperature. Comparing semiconductors to insulators, E_g in semiconductors are much smaller in size compared to that of insulators. Typically semiconductors have 0 eV $< E_g <\sim$ 5 eV, while insulators have $E_g >\sim$ 5 eV. Because of the smaller E_g in semiconductors, thermal energy, for example at room temperature, can be enough for electrons to be excited and make the semiconductor conductive for low-E_g semiconductors.

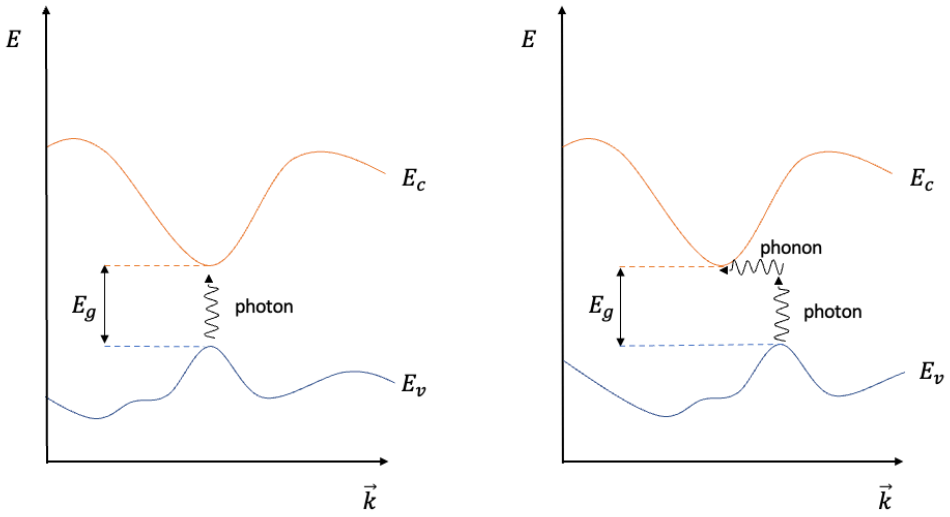

(a) Direct bandgap (b) Indirect bandgap

Figure 2.4: Band structure of a direct and indirect bandgap. The excitation of an electron requires a photon in direct bandgaps, while both an incident photon and phonon are required in indirect bandgaps.

In a real semiconductor, the valence- and conduction bands are not flat, but vary depending on the **k**-vector, also called wave-vector, describing the momentum of an electron. The fact that the energy of en electron is dependent on it's momentum, is a result of the periodic structure of the semiconductor crystal. Based on the location of the valence band maximum (VBM) and the conduction band minimum (CBM), relative to the **k**-vector, bandgaps are either considered direct or indirect. What characterize a direct semiconductor is that the CBM and the VBM are associated with the same **k**-vector, while for indirect semiconductors, the bands extremes occur at different **k**-values, illustrated in figure 2.4. The difference in **k**-vector gives semiconductors with an indirect bandgap a lower probability for exciting electrons from E_v to E_c, as this, in addition to an electron absorbing a photon, also needs a quantified lattice vibration, phonon, to change the momentum of the electron. Considering the lower probability of electron excitation in indirect bandgaps, direct bandgap semiconductors have proven to be more effective in the case of solar cells.

2.2.2 Charge Carriers

For a material to be conducting, charge carriers are essential, with electrons and holes as the two types of charge carriers responsible for current in semiconductors. The conductivity arises as a result that electrons and holes are charged particles free to move inside the material, holes being the absence of electrons and can be considered as a charge carrier with positive polarity. In a semiconducting material, charge carriers and hence conductivity can be achieved by excitation of electrons from E_v to E_c. For electrons to be excited from E_v to E_c, the electrons need an energy supplement equivalent to or larger than the semiconductors E_g energy. This mechanism leaves an empty, positive, conducting hole in the otherwise full valence band E_v and a negative, conducting electron in the otherwise empty E_c. Creating

pairs of electrons and holes in this way, is called to generate electron-hole pairs (EHP's). Absorption of light or thermal energy are examples of mechanisms that can excite electrons from the E_v to the E_c, and thus create EHP's in semiconductors.

For undoped semiconductors the number of charge carriers depends on the properties of the material e.g., bandgap, temperature and the effective masses of the electrons and holes. Such undoped materials are called intrinsic and have no charge carriers at 0 K, as the valence band is filled with electrons while the conduction band is empty. At higher temperatures or other forms of applied energy, EHP's can be generated, if the electrons in the valence band gain energy that is equal to or bigger then the E_g energy. As the charge carriers are generated in pairs, the concentration of electrons (n) is equal to the concentration of holes (p) in intrinsic materials, called the intrinsic carrier concentration, n_i. In situations where n is not balanced by p, and thus equation 2.3 is not true, the material is said to be extrinsic.

$$n = p = n_i \tag{2.3}$$

To increase the amount of charge carriers, doping is often an effective method. By doping a material, small amounts of impurity atoms are intentionally added to the semiconductor material. Doped semiconductors are called extrinsic and the impurities created by doping is therefore called extrinsic dopants. If the foreign atoms have a different valency, number of electrons in the outermost shell compared to the host material, additional energy states is created in the bandgap to accept or donate an electron from the valence or conduction band respectively. These dopants, i.e. donors and acceptors, create states in the bandgap, as showed in figure 2.5.

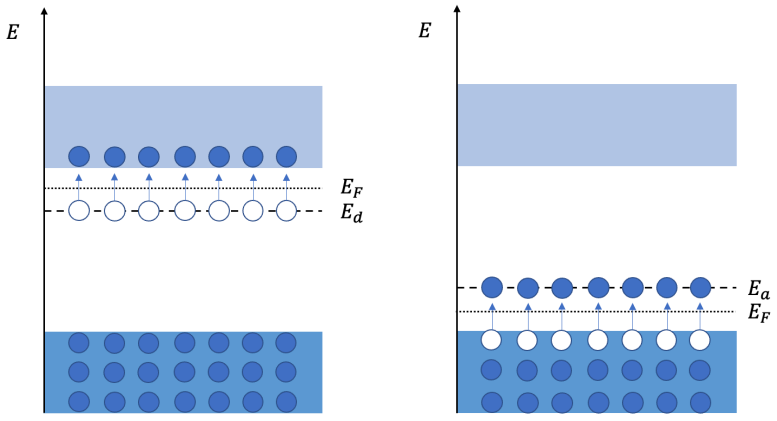

(a) n-doped (b) p-doped

Figure 2.5: Introduced energy states in a n-doped and p-doped semiconductor.

If the impurity atom has one or more additional valence electrons compared to the host atom, it is called donor doping and lead to n-type conductivity. In this type of doping the foreign atoms have additional outer electrons that are unbound and can be excited

with relatively little energy into the conduction band. Thus, in n-doped semiconductors the donor energy level, E_d is close to the conduction band edge as showed in figure 2.5a. p-type doping showed in figure 2.5b is the exact opposite, where the introduced acceptor has one or more less valence electrons than the host atoms. This lack of an electron causes the dopant to accept an additional outer electron, thereby leaving a hole in the valence band. The introduced acceptor level, E_a, is located closer to the valence band for p-doped semiconductors.

Fermi-Dirac statistics is a quantum mechanical description of the energy distribution for fermions, such as protons, neutrons and electrons. Electrons in a solid are shown to follow Fermi-Dirac statistics, and the probability of a certain energy level E being occupied by an electron, can therefore be found by the Fermi's distribution function:

$$f(E) = \frac{1}{exp\frac{(E-E_F)}{k_B T} + 1} \tag{2.4}$$

where $f(E)$ is the probability that a state with energy E is occupied by an electron at a temperature T. k_B is the Boltzmann constant and E_F is the Fermi level, where the probability of E_F being occupied by an electron is equal to 0.5. The position of E_F varies with the temperature and eventually doping of the semiconductor. As can be seen in figure 2.6, where E_F is positioned at 0.0 eV, all energy states at 0 K with $E < E_F$ are occupied by electrons, while the energy states with $E > E_F$ are unoccupied. Resulting in a full VB and empty CB, and a non-conducting semiconductor without any free charge carriers at 0 K. If the temperature is increased above 0 K, the probability of occupation for states above E_F is increased as a result of additional energy, leaving states below E_F empty.

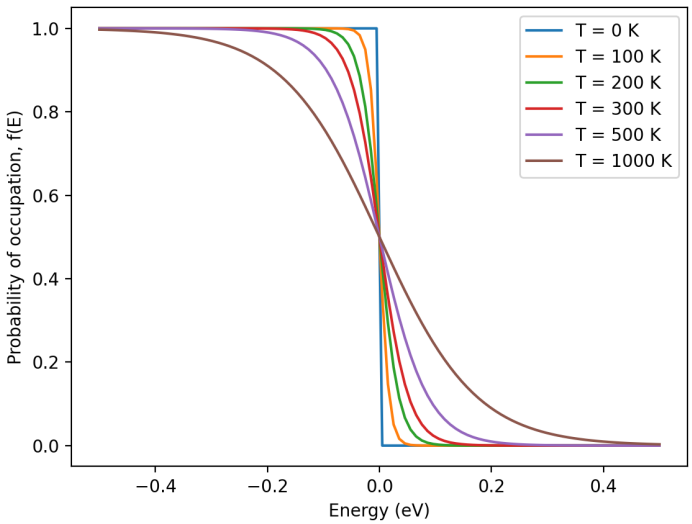

Figure 2.6: The Fermi-Dirac distribution function at different temperatures showing the probability of an energy state being occupied by an electron. All energy states up to E_F are occupied at 0 K.

2.2.3 Defects

Crystalline structures have a three-dimensional periodicity of identical building blocks. If the atom arrangement is perfectly ordered, it is called an ideal crystal, but in real life crystals will always have imperfections and impurities. A common term for any deviation from the perfectly arrangement in a crystal is defects. Defects in crystalline solids can in many cases actually functionalize the semiconductors, where important properties of crystals are in fact controlled as much by imperfections as by the composition of the host crystal. It is therefore necessary to know what types of defects that form, and which role they play, in order to understand the behavior of solids.

Based on dimension, defects in semiconductors can be categorized into four different groups: zero-, one-, two- and three-dimensional. Zero-dimensional defects, also called point defects, occur only at or around one single lattice point. These defects typically involve at most a few extra or missing atoms. Defects along a one-dimensional line is called line defects or dislocations, and may cause or relieve crystal strain. A discontinuity across a two-dimensional plane is referred to as a planar defect. These types of defects normally separate regions of the materials that have different crystal structures and/or crystallographic orientations, and are therefore found at surfaces, grain boundaries or interfaces. Lastly, are the three-dimensional defects, often called bulk-defects or volume-defects. They generally occur on a much larger scale than the microscopic defects, and include cracks, pores and other phases.

All materials above 0 K contain point defects, as it is a thermodynamic necessity. Regardless, if a semiconductor is intrinsic or extrinsic, the defects have a dramatic effect on the material properties. The conductivity for some semiconductors is entirely due to trace amounts of chemical impurities. For other materials the color and luminescence arise from impurities or imperfections in the crystal. Imperfections can accelerate atomic diffusion or govern the mechanical properties of materials. When it comes to light-emitting diodes and solar cells, especially those utilizing new materials, managing the amount of defects can boost their efficacy, hence it is important to understand defects at a fundamental level.

2.3 Thin Film Growth

Thin films are thin layers of a material with thickness ranging from a single monolayer of atoms up to 2 microns. Applying a thin film to a substrate is usually called thin film deposition, and there are many different techniques that can be used for this process. Depending on whether the deposition of material is in solid or reactive gaseous form, it is categorized as a physical or chemical process. Some well-known chemical deposition techniques are chemical vapor deposition, CVD, and plasma enhanced CVD (PECVD) where it occurs a chemical reaction between the gaseous molecules and the substrate surface. Sputtering, molecular beam epitaxy (MBE) and electron beam evaporator are widely used physical processes where atoms are moved from a source or target and deposited on the

substrate.

There are three different modes in which thin films grow; Frank-van der Merwe mode, Volmer-Weber mode and Stranki-Krastanov mode. Frank-van der Merwe mode is also known as layer-by-layer growth. This type of growth occurs when the deposited atoms are more strongly bound to the substrate than to each other, resulting in atoms forming single monolayers on the surface before forming a second layer. For this to happen, it requires a lattice matching between the substrate and the layer growing on it. Volmer-Weber mode, also called island growth, have adatoms forming three-dimensional groups/islands on the substrate surface. This occurs when the deposited atoms are more strongly bound to each other than to the surface, typically when there is a large lattice mismatch. Stranki-Krastanov mode is a combination of the two modes mentioned. This mode is also known as layer-plus-island growth. Here it is more energetically favorable for atoms to form island after one or a few monolayers are formed.

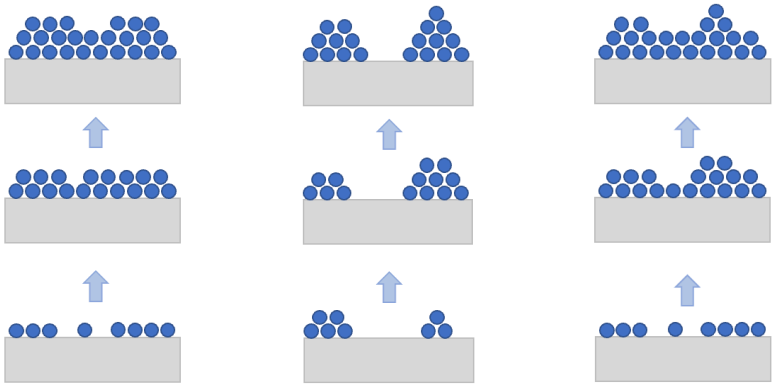

(a) Frank-van der Merwe (b) Volmer-Weber (c) Stranki-Krastanov

Figure 2.7: Illustration of different growth modes. Frank-van der Merwe (layer-by-layer growth), Volmer-Weber (island-growth) and Stranski-Krastanov (layer-plus-island).

During discussions of thin film deposition, epitaxial growth is often mentioned. Epitaxial growth is when the deposited film grows with a particular orientation determined by the single crystal substrate. The choice of substrate thus become incredibly important and decisive, and this type of growth tend to result in high crystal quality, precisely because of the relation to the substrate. Epitaxial growth are often divided into homoepitaxial- and hetroepitaxial growth, where the film and the substrate are the same material and the film and the substrate are different materials, respectively. Epitaxial growth does not require complete lattice match, but that the film and substrate is similar enough to interact and have a defined relationship. Lattice mismatch between the substrate and the thin film can cause stress or strain, which further can develop to defects and dislocations. In some cases lattice mismatch can generate a highly dislocated region within a few hundred nanometers from the interface to relieve lattice strain, and therefor affect the quality of the thin film. In this work hetroepitaxial growth of $ZnSn_xGe_{1-x}N_2$ have been pursued to have good material

quality, but the growth quality also strongly dependent on the choice of substrate.

2.4 II-IV-N's

Binary III-nitrides such as GaN, InN and AlN are today one of the most important groups of materials in optoelectronics, and widely used in applications like LED, photo detectors and solar cells. As a result of the materials having bandgap energies ranging from the infrared to the ultraviolet part of the electromagnetic spectrum [17], alloys of these III-nitrides e.g., InGaN, have the ability to collect a major part of the solar energy. Despite the superior properties, III-nitrides also have some disadvantages related to cost, large scale production and phase segregation. Materials like In and Ga are expensive and not earth-abundant, and the materials and alloys typically require expensive grow techniques, which gives limitations for large-scale production. Additionally, the large lattice mismatch between GaN and InN gives rise to phase segregation for In-rich alloys, reducing the ability of the $In_xGa_{1-x}N$ to cover the full visible spectrum.

The II-IV-nitrides is a group of novel earth-abundant semiconductors promising for the next-generation solar cells and other optoelectronic devices, found to possess many of the same properties as the III-nitrides. For the II-IV-N_2's, the III-element (e.g. Ga in GaN) is substituted with 50% II-elements (Zn) and 50% IV-elements (Sn, Ge, Si). Ternary systems, such as $ZnSnN_2$ and $ZnGeN_2$, have showed to adapt a wurtzite-like crystal structure from the III-nitrides, where the elements in these Zn-IV-N_2's are earth-abundant and therefore a favorable alternative to the conventional III-nitrides. Another advantage, compared to the III-nitrides, is that the II-IV-N_2's typically can be grown with techniques that is cheaper and easier to scale, such as for example sputtering.

As the cation in III-nitrides is replaced with two heterovalent cation elements in II-IV-nitrides, it becomes necessary to consider cation disorder and stoichiometry. Cation disorder is a phenomenon commonly observed in II-IV-nitrides, which refers to deviations in the atomic positions within the cation sublattice from an ordered crystalline arrangement. Meanwhile, the stoichiometry in II-IV-nitrides describes the ratio between the cations, which is expressed as the II/(II+IV) ratio.

2.4.1 $ZnSnN_2$

$ZnSnN_2$ is an emerging ternary nitride semiconductor due to it's many similarities to the III-nitrides. The material is earth-abundant, non-toxic, and have a high absorption coefficient [18]. It's bandgap aligns with the requirements for photovoltaic applications (PV), particularly as a solar absorber, making it a promising candidate as, e.g., a top cell in tandem solar cells. $ZnSnN_2$ is experimentally found to crystallize in three different structures. The most energetically favorable structure for $ZnSnN_2$ is the orthorhombic $Pna2_1$, but orthorombic $Pmc2_1$ structure have also been identified as possible, but so far not observed experimentally. In addition, $ZnSnN_2$ can also be synthesized in the

hexagonal wurtzite $P6_3mc$ and monoclinic structures [2]. The preferred structure will depend on the substrate lattice-matching and the growth conditions [18] [2]. However, the temperature-window for single crystalline growth of $ZnSnN_2$ is relatively narrow. As an example, using magnetron sputtering, Gogova *et al.* [19] showed single crystalline growth of wurtzite $ZnSnN_2$ on ZnO substrates, with a lattice mismatch of 4.2%, at 350 °C . The epitaxial relationship to the ZnO substrate and wurtzite crystal structure of $ZnSnN_2$ was later supported by employing phi scans, showing a six-fold symmetry of the hexagonal crystal combined with low dislocation density, by Olsen *et al.* [2].

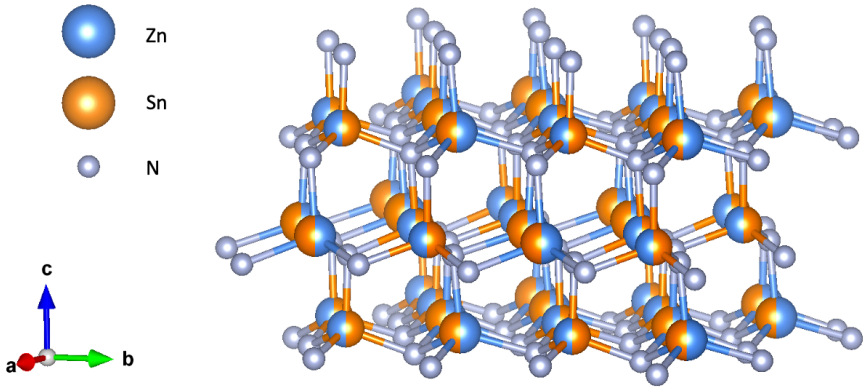

Figure 2.8: Fully disordered $ZnSnN_2$ in a wurtzite-like structure.

Experimental studies show large variations in the measured optical and electrical properties for $ZnSnN_2$, with optical bandgaps ranging from $1.1 - 2.4$ eV [18], carrier concentrations in the range 10^{16} – 10^{21} cm^{-3} [18] and mobilities from $0.5 - 22.7$ cm^2 $V^{-1}s^{-1}$ [18]. These large variations can originate from the fact that the optoelectrical properties are affected by factors, such as the crystal structure, defect density, Zn-Sn stoichiometry and cation-disorder [18]. Despite the varying bandgap values, high quality crystalline wurtzite $ZnSnN_2$ have shown a direct bandgap of ∼1.7 eV [2], an optical bandgap that is well suited for the top cell in a tandem solar cell together with Si.

Unfortunately, $ZnSnN_2$ also have some challenges, which currently limits the use of the material. Unintentionally doped $ZnSnN_2$ exhibits n-type conductivity, with a very high as-grown carrier concentration. As-grown stoichiometric $ZnSnN_2$ typically exhibits n the range of $2.10 \times 10^{19} cm^{-3}$ - $1.85 \times 10^{20} cm^{-3}$ [20], which can pose challenges and a degenerate behavior [2, 20]. A degenerate semiconductor is a semiconductor with such a high level of doping that the Fermi level lies within the conduction band, making the material acting more like a metal than as a semiconductor. The degenerated behavior can potentially shift the optical bandgap due to the Burstein-Moss effect, a phenomenon where the optical bandgap of a material is increased due to electrons occupying a significant amount of states in the conduction band [18]. Importantly, the degenerate behavior also makes a pn-junction diode non-rectifying, typically due to tunneling effects, allowing charge to flow in both directions, which in the context of solar cell devices is an undesirable function.

Li doping has been attempted to reduce the carrier concentration, by substituting Li for Zn as shallow acceptor defects [20]. Unfortunately, the carrier concentration in $ZnSnN_2$ seemed to be unaffected by the doping concentration. Even though the defects causing the high carrier concentration in $ZnSnN_2$ are still not fully understood, theoretical calculations employing density functional theory (DFT) have been used to calculate the formation energy of the defects, i.e, the probability of the defects being present. The work presented by Chen *et al.* [21] indicate that the tin-zinc antisites (Sn_{Zn}) are expected to be the dominating donor defect. Other intrinsic donor defects that may occur in the material are nitrogen vacancies (V_N) and zinc interstitials (Zn_i). In addition to the intrinsic defects, extrinsic defects are often incorporated during growth. Extrinsic defects, where nitrogen can be substituted with both oxygen and hydrogen (O_N) (H_N), or hydrogen can take interstitial positions (H_i), is predicted not to have as a significant effect on the charge carrier concentration compared to that of (Sn_{Zn}). Off-stoichiometric growth have shown to be an approach to reduce the charge carrier concentration [7]. By making Zn-rich samples, the probability that Zn substitutes for Sn is increased, creating double acceptor (Zn_{Sn}) antisites. Correspondingly, will the high concentration of Zn in relation to Sn decrease the probability of forming (Sn_{Zn}), assumed to be the most dominating donor defect.

2.4.2 $ZnGeN_2$

$ZnGeN_2$ is another ternary nitride compound with a great potential as an earth-abundant and low toxicity light-absorbing material. The curiosity in the Zn-IV-nitride alloys first arose in the 1970s, when $ZnGeN_2$ was of interest as an alternative to GaN [5]. $ZnGeN_2$ is reported to crystallize in similar structures as $ZnSnN_2$, where the wurtzite-like is the most reported structure [22, 23]. In wurtzite-like structures there are two possibilities of ordering the cation lattice that preserves the octet rule [24]. The orthorombic $Pna2_1$ structure have two cation sites and two anion sites, which could attain fully ordered cations. There are also experimental reports of $ZnGeN_2$ crystallizing in the wurtzite space group $P6_3mc$, as a consequence of fully disordered cations. Where the hexagonal wurtzite structure only have one position for cations and one for anions, meaning that cations are simply randomly distributed.

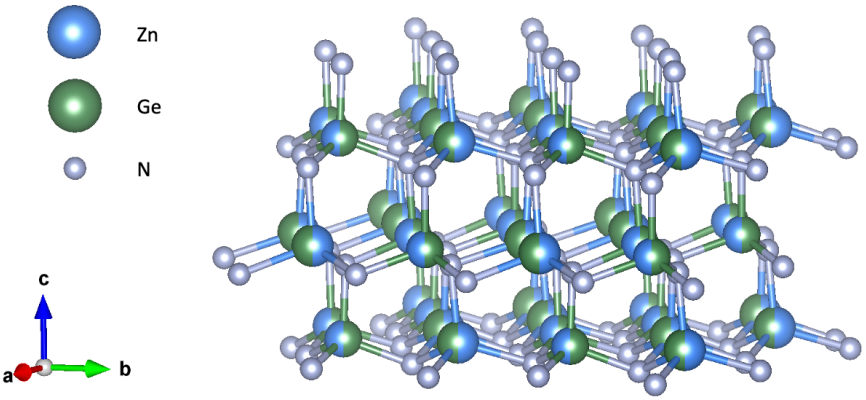

Figure 2.9: Fully disordered $ZnGeN_2$ in a wurtzite-like structure.

There are several studies that have examined the effect growth temperature and post-growth annealing have on the cation disorder in II-IV-nitrides. For instance, in polycrystalline $ZnGeN_2$ the degree of ordering was found to increase with growth temperature [24]. The growth temperature and the cations disorder have a distinct influence on the materials structure, which, in turn, is shown to affected the optical bandgap. Studies have demonstrated control of cation site ordering by using variable growth temperatures and post-growth annealing for bulk samples, suggesting that cation disorder can reduce the bandgap [22, 25]. However, for optically active materials, minimizing defects is necessary to ensure crystal quality, and well-crystallized films have shown heteroepitaxial $ZnGeN_2$ [26].

$ZnGeN_2$ is, similarly to $ZnSnN_2$, an n-type semiconductor, but exhibit a significantly lower carrier concentration for comparison. The lower carrier density prevents the occurrence of degenerate behavior, which is absolutely crucial not to have for a semiconductor material used in a pn-junction. Optical studies on $ZnGeN_2$ have shown that it has a direct bandgap [27] [28], which is ideal for optoelectronic applications. It's bandgap energy is around 3.1 eV [2, 29], considerably higher than the optimal bandgap size of ~ 1.7 eV found for $ZnSnN_2$. Overall, $ZnGeN_2$ possesses a lower and more controllable carrier concentration better suited for solar cells then $ZnSnN_2$. However, the roles are reversed when it comes to bandgap, where $ZnSnN_2$ have a optimal bandgap size for tandem cell applications, while $ZnGeN_2$ has a bandgap that is too high for efficient use with Si in a tandem configuration.

2.4.3 $ZnSn_xGe_{1-x}N_2$

$ZnSnN_2$ and $ZnGeN_2$ can be combined into a quaternary alloy. $ZnSn_xGe_{1-x}N_2$ semiconductor alloys have a crystal structure and electronic structure similar to that of InGaN alloys, where $ZnSnN_2$ is analogous to InN and $ZnGeN_2$ is analogous to GaN. Based on the fact that $ZnSnN_2$ and $ZnGeN_2$ possess different suitable qualities, $ZnSn_xGe_{1-x}N_2$ films with $0 \leq x \leq 1$ can be tuned by gradually substituting germanium with tin. Unlike InGaN alloys, which suffer from phase segregation beyond $\sim$ 20% In, $ZnSn_xGe_{1-x}N_2$ forms a continuous alloy for the entire range of $0 \leq x \leq 1$ [30]. $ZnSn_xGe_{1-x}N_2$ is a direct bandgap semiconductor, with it's bandgap tunable from around 2 eV (for $ZnSnN_2$) to 3.1 eV (for $ZnGeN_2$) by controlling the Sn/Ge ratio [4]. The alloy has a calculated lattice mismatch of 5% for $ZnSnN_2$ and $ZnGeN_2$, which is smaller than the 10% for InN and GaN, and has been shown to be stable against phase separation [5], giving it an advantage compared to InGaN. Overall, $ZnSn_xGe_{1-x}N_2$ materials offer tunability of the bandgap and the electrical properties, which makes them highly attractive as light absorbers in solar cells.

2.5 pn-Junction

A pn-junction can be made from a single crystal having two regions with different conductivity (p and n), where the interface between a p-type and a n-type semiconductor creates a pn-junction. A pn-junction is the basis for constructing devices like diodes, transistors, and solar cells, where they play a critical role in controlling the current flow. Figure 2.10 shows

a simple illustration of a junction.

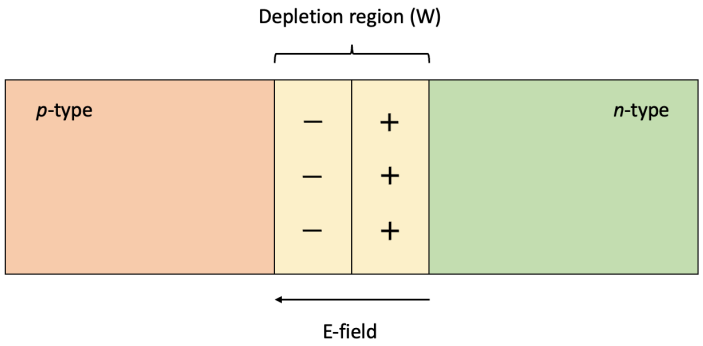

Figure 2.10: Illustration of a pn-junction, showing the depletion region, W, created at the interface between the p-type doped and n-typed doped region. The uncompensated ions generate an electric field over W.

As a result of the opposite doping, there will be a concentration gradient for both charge carriers over the junction, which will lead them to diffuse over the junction. As electrons from the n-side and holes from the p-side diffuse from one region to another, they leave uncompensated ions behind. On the n-side, positive space charge from donor impurity atoms occure. Oppositely, will negative space charge, acceptor impurity atoms, arise on the p-side. Due to the charge difference of the uncompensated ions an electric field (E) is created over an area close to the junction called the depletion region (W). The electric field will have an opposite effect on the charge carriers as the concentration gradient leading to diffusion. The drift current caused by E and the diffusion current will at a certain point cancel each other, leaving no net current at equilibrium. Equation 2.5 shows the current density for electrons, J_n, and holes, J_p, where the first term describes the drift current and the second term describes the diffusion current. At equilibrium these terms cancel each other out.

$$J_n = q\left[\mu_n n(x)E(x) - D_n\frac{\partial}{\partial x}n(x)\right], \quad J_p = q\left[\mu_p n(x)E(x) - D_p\frac{\partial}{\partial x}p(x)\right] \tag{2.5}$$

For a pn-junction at equilibrium the Fermi level is always constant over the junction. Doping a semiconductor shifts the Fermi level opposite for a p-type and a n-type semiconductor, and a band bending occurs within the depletion region, as shown in figure 2.11. The size of W depends on the doping concentration and any applied bias. The vertical axis in figure 2.11 represents increasing electron energy, and oppositely decreasing hole energy. Hence, the band bending implies that a supply of energy is needed to move either of the charge carriers to the opposite side of the junction. This difference in energy between the bands is often referred to as a potential barrier or the built-in potential, V_{bi}.

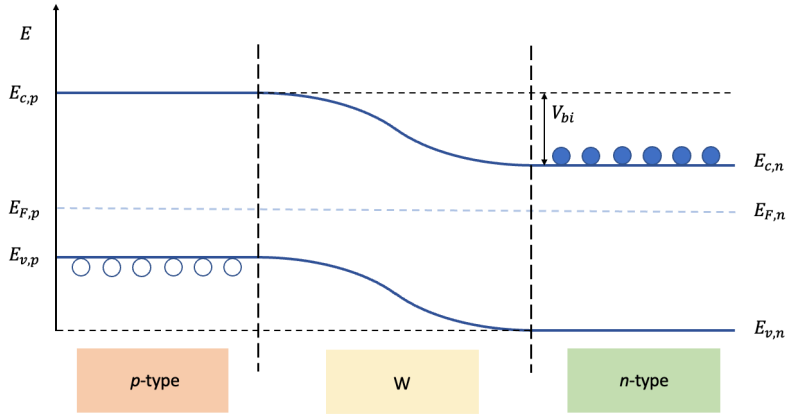

Figure 2.11: Bandstructure of a pn-junction illustrating a constant Fermi level, E_F, and band bending of the conduction band, E_c, and valence band, E_v.

For an electron or a hole to overcome the potential barrier, it needs additional energy equivalent to the barrier, qV_{bi}, where q is the particle charge. By applying a voltage over the junction the potential barrier can be increased or decreased. The outcome of applying a revers bias to the pn-junction is an increase of the electric field. A higher electric field at the depletion region will further increase the potential barrier, and therefore decrease the probability for charge carriers to overcome the barrier. Applying a forward bias will on the other hand reduce the electric field and the potential barrier, and by that increase the chance of charge carriers overcome the barrier.

$$V_{bi} = \frac{k_B T}{q} ln \frac{N_d N_a}{n_i^2} \tag{2.6}$$

Equation 2.6 shows the relation between the doping concentrations and V_{bi}, where N_d is the donors in the n-type and N_a is the acceptors in the p-type.

The pn-junction is the most widely used structure for solar cells, but is also the basis of other electric devices such as diodes, LED's, transistors and lasers.

2.6 Working Principles of Solar Cells

A solar cell is an optoelectrical device that converts solar radiation into electricity by the photovoltaic (PV) effect. The basic structure of a solar cell is semiconductor materials in the form of a pn-junction, were most of today's solar applications are made from crystalline Si. As light shine on a solar cell it produces both a current and a voltage to generate an electric power. This requires a material that by absorption of light raises an electron to a higher energy state, and secondly separates the generated charge carriers so that they can move in an external circuit where they can generate a current.

The sun emits light with a wide range of wavelengths, spanning the ultraviolet, visible

and infrared region of the electromagnetic spectrum. Light can be seen as particles called photons, which have the energy $E = \frac{hc}{\lambda}$, where h is Planck's constant, while c and λ is the velocity and the wavelength of the light. When a solar cell is illuminated, photons with higher energy than the materials bandgap, i.e., $E \geq Eg$, will excite charge carriers. The bandgap of a PV semiconductor is therefor an important property and crucial for which wavelengths of light the material can absorb and convert to electrical energy. As light with sufficient energy reaches the depletion region EHP's are generated, separated and further swept out of the depletion region by the electric field. This causes the concentration of electrons on the n-side and holes in p-side to becomes so high that a potential difference is developed between them. If a load is connected between the two regions, electrons will start to flow through the load. The electrons will recombine with the holes in the p-region, and in this way a solar cell continuously provides direct current as long as it is illuminated.

The net current density in a illuminated cell can be described by the diode equation

$$J(V) = J_{sc} - J_{dark}(V) = J_{sc} - J_0(e^{qV/k_BT} - 1) \tag{2.7}$$

where J_{sc} is the short current density, which is the current density that flows through the solar cell when the voltage across the cell i zero. J_{dark} is the dark saturation current and flows in the opposite direction of J_{sc}. Unlike the short current, the dark current is generated by thermal excitation rather than by the absorption of photons from light. J_0 is the saturation current, which is a constant.

Maximum voltage over the solar cell is reached when $J_{sc} = J_{dark}$, and is called the open-circuit voltage, V_{oc}. This is the voltage across the solar cell when there is no external load connected to it.

$$V_{oc} = \frac{kT}{q} ln \left(\frac{J_{sc}}{J_0} + 1 \right) \tag{2.8}$$

The efficiency is an important parameter for optimizing the performance of solar cells, and is determined by the ratio between the amount of electrical power produced by the cell (going out) compared to the energy from the light shining on it (coming in).

$$\eta = \frac{P_{out}}{P_{in}} \tag{2.9}$$

The efficiency is limited by several factors, among other things the quality of the pn-junction, the bandgap of the semiconductor material and the reflection of the solar cell surface. There is a theoretical maximum efficiency for a solar cell consisting of a single pn-junction, called the Shockley-Queisser limit

$$\eta_{limit} = \frac{E_g}{qV_{oc} - 1} \tag{2.10}$$

The power delivered by a solar cell is given by the product of the operating voltage and the associated current. The maximum power is thereby achieved when both the current and

voltage are at their maximum points

$$P_{out} = J_{max}V_{max} \tag{2.11}$$

Fill factor (FF) describes the ratio of the maximum power output of a solar cell to the product of it's short-circuit current density and open-circuit voltage, and is given by

$$FF = \frac{J_{max}V_{max}}{J_{sc}V_{oc}} \tag{2.12}$$

FF is a measurement of the squareness of the J-V curve, meaning the largest area of a rectangle which will fit under a J-V curve. FF is crucial for the efficiency of the solar cell and can be put into equation 2.9

$$\eta = \frac{J_{sc}V_{oc}FF}{P_{in}} \tag{2.13}$$

The main components of a solar cell is the substrate, called the absorber, and the top layer, the emitter. A typical solar cell design consists of a thin emitter layer grown on a relatively thicker absorber, where the absorber and the emitter are oppositely doped and form the pn-junction. The absorber absorbs the majority of photons causing electrons to be exited into the conduction band. On the other hand, the emitter extract the separated charges and collects them into a photocurrent. It is important that the contacts on the surface of the cell do not obstruct light to reach the emitter, and that the emitter layer is thin enough so that the solar radiations reach the depletion region of the cell. A current collecting contact is also placed at the bottom of the absorber layer. The surface is often covered with anti-reflective coatings, as well as a thin protective glass.

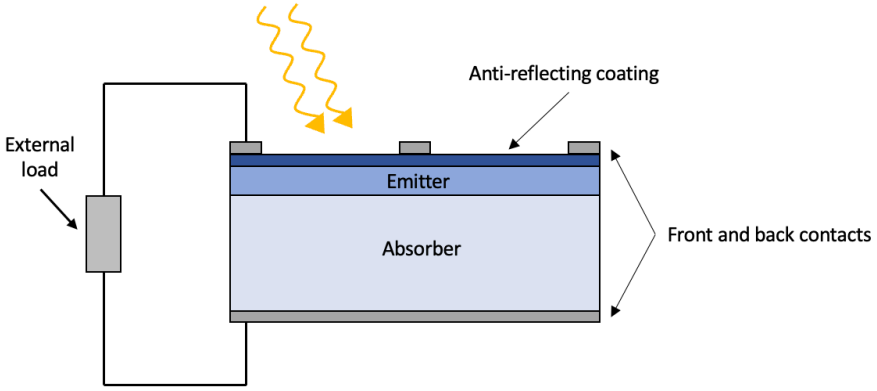

Figure 2.12: Simplified illustration of a single junction solar cell.

Currently the solar industry is dominated by single-junction crystalline (c-Si) based on reasons such as non-toxic behavior, earth abundancy and the fact that they exhibits good reliability. The Si industry has developed for over seven decades and dominated the electronics market. Si solar cells are a well-developed solar technology holding more than

95% share of the photovoltaic market with efficiencies over 26% [1]. Still it has yet to reach the Shockley-Queisser limit of 33.15% for single-junction devices. On the basis that Si has an indirect bandgap, while direct bandgaps are better suited for solar cells due to a more rapid absorption of the light, makes research on other material still interesting despite the Si-dominance. One reason for the low Shockley-Queisser limit is that all solar radiation with photon energies smaller than the bandgap will not be able to excite electrons and simply pass through the material. Photon energies higher than the bandgap will excite the electrons above the conduction band edge, where the excess energy is dissipated through the crystal as heat. Tandem solar cells are designed to capture more of the solar energy and are therefor an exiting and favorable technology.

2.6.1 Tandem Solar Cells

One method to increase the efficiency of solar cells and surpass the Shockley-Queisser limit for single-junction devices is the use of tandem solar cells (TSC's). The basic principal of TSC's is to stack several materials with different bandgaps on top of each other, and by that obtain a wider absorption spectrum and a more efficient utilization of the photon energy compared to the regular single-junction solar cells. The top cell, containing the highest bandgap, will absorb the higher energy photons and letting the lower energy photons pass through to the bottom cell. The bottom cell have a lower bandgap than the top cell, and will by that be able to absorb lower energy light. This process allows a maximum number of photons to be harvested by utilizing a broad solar spectrum.

The two most common configurations of TSC's connects the cells using two or four terminals, illustrated in figure 2.13. In the two terminal (2-T) device, shown in figure 2.13a, the two cells are connected in series, where the top cell is directly fabricated on top of the bottom cell. This results in the total generated current being limited to the lowest-performing cell. In addition, the requirement of current matching between the two cells connected in series imposes limitations to the bandgap range of the top cell. For a TCS with a *c*-Si bottom cell the ideal top cell bandgap is constrained to a narrow range of 1.7 - 1.8 eV. The four terminal (4-T) design are similarly to the 2-T design vertically stacked cells, but in contrast each cell has it's own separate two terminals, shown in figure 2.13b. The cells are therefore optically coupled, but electrically independent, so they can be operated and optimized separately. This opens up the bandgap range of the top cell, and for a bottom cell of *c*-Si one can achieve high efficiencies over a wide bandgap range of 1.6 - 2 eV.The disadvantage of the 4-T design is the dependency of more than one transparent electrode, which may cause more parasitic absorption. Compared to 2-T TSC's this might increase the overall cost in the fabrication process and the requirement of more electrical components (e.g. several inverters), making the 2-T design more suitable for large scale production.

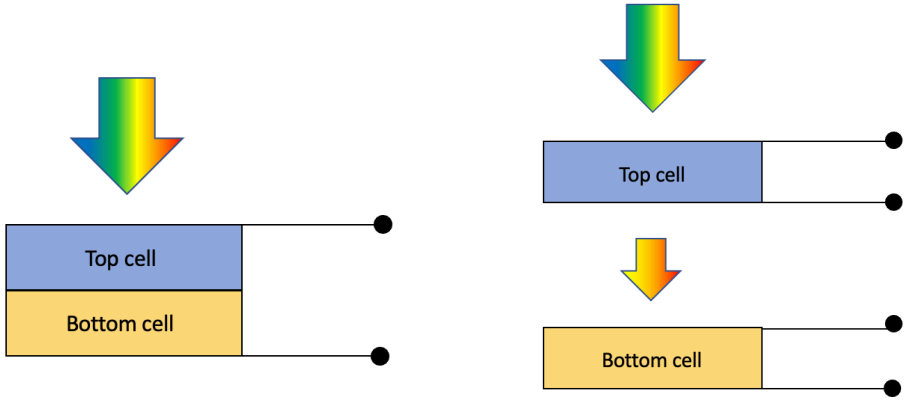

(a) Two terminal (2-T) (b) Four terminal (4-T)

Figure 2.13: Two terminal (2-T) and four terminal (4-T) configuration of a two-junction tandem solar cell.

According to the article written by Ehsan Raza and Zubairr Ahmed [1], *c*-Si is the ideal choice for a bottom cell due to their cost competitive manufacturing. Their market dominance is also a result of a high open-circuit voltage (V_{oc}) of up to 0.75 V [31], high efficiency [32], and suitable bandgap (1.1 eV) [33]. By the fact that the bandgap of the top cell is dependent on the bottom cell, various materials have been proposed for the top cell in tandem solar cells. A top cell material needs to be transparent to light of longer wavelengths, have a high carrier mobility and a suitable carrier concentration. In addition to the physical requirements, it is desirable that the material also is earth-abundant, cheap, non-toxic and suitable for large-scale production. In this research $ZnSnGeN_2$ alloys are examined as a potential top cell candidate in Si-based TSC, and since a 2-T configuration is the most likely to be used, $ZnSnGeN_2$ are aimed to have a bandgap of $\sim$1.7 eV.

Chapter 3

Experimental Methods

The aim of this chapter is to give insight to the experimental methods used in this work. Section 3.1 addresses the sputtering deposition, a well-known deposition technique, used to deposit all the thin films in this thesis. This section is based on the textbook of Campbell [34]. Section 3.2, based on the textbooks of Karishnan [35] and Leng [36], presents the SEM EDS technique employed to identify elemental compositions. Section 3.3, based on the textbook of Leng [36], introduces X-Ray Diffraction as the method used to determine structural properties. For examining the electrical properties, Hall effect is employed, based on the textbook of Streetman [11], while UV-VIS Spectroscopy, based on the textbook of Karishnan [35], is used to investigate optical properties. Finally, Section 3.6 and 3.7 provides a brief description of SIMS and FTIR techniques, drawing from the textbooks of Leng [36] and Karishnan [35], respectively.

3.1 Sputtering Deposition

Sputtering is a widely utilized method for depositing thin films. During a sputtering process, a target material is bombarded with plasma ions, with enough energy to knock atoms out of a target with a known composition. These sputtered atoms or molecules then travel in a vacuum environment and deposit onto a substrate, that is typically placed a few centimeters away from the target, to form a thin film. Sputtering can be carried out under various conditions, such as with or without a magnetic field, with different gas pressures, and using different target materials. The specific sputtering deposition method used depends on the desired properties and requirements for the deposited thin film. In the microelectronics industry, sputtering is commonly used to deposit thin films of metals, alloys, or insulators onto Si wafers or other substrates. Sputtering is considered to be an important technique for depositing high-quality thin films with precise control over their properties and a valuable tool for large scale production of thin films.

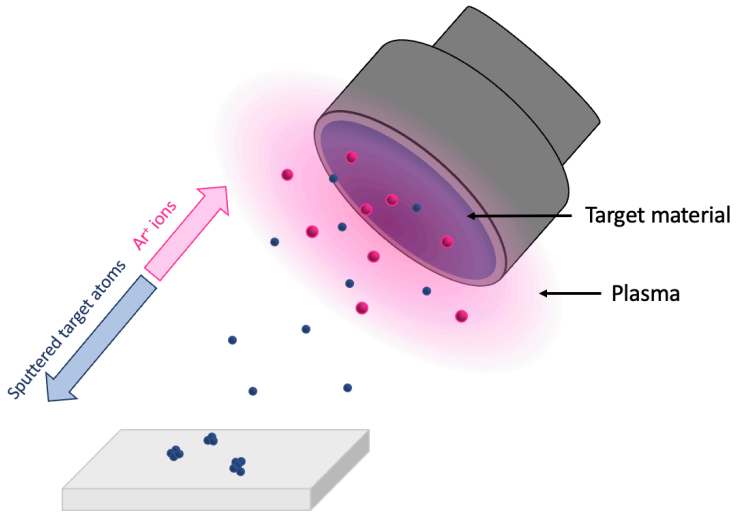

Figure 3.1: Illustration of a sputtering process where accelerated Ar^+-ions (pink) hit the target material and eject target atoms (blue). Figure adapted from Olsen [37]

3.1.1 Sputtering Process

The sputtering process takes place inside a low vacuum chamber, typically referred to as the sputtering chamber. Inside the sputtering chamber one or more targets are angled in the direction of the substrate. A cathode is often located behind the target, while a shield around the target acts as the anode. An inert gas, often argon (Ar), is introduced into the chamber. By applying a high enough voltage between the two terminals, a plasma will be generated in front of the target material, as the Ar-gas is ionized, resulting in Ar^+-ions and free electrons. Inert gases like, Ar, are typically used to induce plasma as they avoid interfering with the formation of the thin film.

The sputtering technique further involves bombarding the target material with plasma ions. The high-energy Ar^+-ions are accelerated by the applied voltage towards the negatively charged cathode, bombarding the target material. When the ions collide with the target material, they transfer their energy to the atoms or molecules in the material, causing them to be ejected from the surface. These ejected atoms or molecules are then deposited onto a substrate to form a thin film. During the sputtering process, as the high-energy ions sputter of target atoms, also secondary electrons are generated and ejected from the target material. Due to the negative charge of the secondary electrons, they experience an opposite influence by the electrical field in the plasma, compared to the Ar^+-ions. The secondary electrons are accelerated through the plasma, away from the target. These electrons can collide and ionize another neutral gas atom, leading to additional sputtering. The plasma is thus self-sustaining as long as the chamber is biased and the voltage is sufficiently high to accelerate both ions and electrons to a satisfactory degree.

3.1.2 Magnetron Sputtering

Magnetron sputtering is a technique that uses a magnetic field to enhance the sputtering rate and increase the efficiency of the process. The magnetic field is used to confine the plasma to a specific area around the target material. This confinement results in a higher ion bombardment intensity on the target, which leads to a more efficient removal of target material and a more uniform film deposition on the substrate.

The magnetic field is created by a permanent magnet behind the target, which generates a magnetic field perpendicular to the surface of the target. Because the magnetic field lines are perpendicular to the surface of the target material, the Lorentz force causes the charged particles in the plasma to spiral around the magnetic field lines and remain near the target material, rather than moving out into the rest of the sputtering chamber. This results in a higher density of plasma near the target material, which increases the efficiency of the sputtering process.

Magnetron sputtering is widely used in the microelectronics and optical industries, due to it's ability for precise control over the deposition parameters and that it is capable of depositing a wide variety of materials, including metals, alloys, ceramics, and insulators. Additionally, magnetron sputtering can be performed under different conditions, such as high- and low pressures, or in reactive gas environments, which allows for deposition of various types of materials, including thin films with tailored properties.

3.1.3 Sputtering yield and deposition rate

Sputtering yield and deposition rate are important parameters in the sputtering process, as they act as a measure of the efficiency of the sputtering process. The sputtering yield (S) refers to the number of ejected atoms or molecules from the target surface (Z_e) per incident ion (Z_i).

$$S = \frac{Z_e}{Z_i} \tag{3.1}$$

Higher sputtering yields generally result in higher deposition rates and a more efficient use of the target material. The deposition rate is the rate at which the target material is deposited onto the substrate, and it is usually expressed in units of angstroms per second (Å/s) or nanometers per second (nm/s). The deposition rate is directly proportional to the sputtering yield, and often used to estimate the thickness of the deposited thin film, and also to control the film properties, such as density and composition. There are several factors that influence the deposition rate and the sputtering yield, among other things, the ion flux and the ability of ejected atoms to travel through plasma, affect the growth rate of the sputtered film.

The quality of the deposited thin film depends on how the sputtered atoms bond to each other and to the substrate atoms. As the sputtered atoms reach the substrate surface, it is the mobility of the adatoms that determines if they are able to reach their most

energetically favorable position during growth. The adatoms mobility at the surface are controlled by the substrate temperature and the binding energy between substrate atoms and sputtered atoms. Having a too low surface mobility, makes the adatoms end up in unfavourable positions, resulting in e.g., amorphous and porous films. By increasing the substrate temperature, and thus the surface mobility, adatoms reach energetically favorable positions and denser films are formed. Mobility of adatoms is also affected by the ion energy, which is a product of target power and chamber pressure, making the mobility affected by the kinetic energy of the sputtered atoms. The composition and stoichiometry of the deposited film can also be controlled by adjusting the power.

There is, however, a threshold for substrate temperature and ion energy, where crossing the limit reduces the quality of the film. Too high substrate temperature can make the deposited material deteriorate, and having too high target power, the structure will suffer continuous damage throughout the deposition.

3.1.4 HiPIMS

HiPIMS (High Power Impulse Magnetron Sputtering) is a sputtering technique used to deposit thin films onto substrates by utilizing short, high power pulses. The high voltage pulses are applied to the target material, where the time interval between the pulses are significantly larger than the duration of the pulses. The extent of the pulses are normally tens to hundreds of microseconds with frequencies up to 5 kHz. By pulsing the applied voltage a larger fraction of the sputtered target material, as well as e.g., reactive gas, are ionized, while the time-average power remains low enough not to overheat the target or the magnetron. The average target power is given by

$$P_{avg} = V_{avg} I_{avg} \tag{3.2}$$

The higher ionization in HiPIMS is due to the pulses accelerating the ions towards the target and secondary electrons with a higher energy. This is especially important in the case of N_2, considering that N_2 bonds are generally more difficult to break then e.g., O_2 bonds. According to Bazioti *et al.* [38], conventional RF/DC sputtering of nitrides can result in N_2 incorporation in the film, in addition to N. HiPIMS also creates a dense plasma that sputters target materials more efficiently than traditional DC or RF sputtering methods, as the high voltage used in HiPIMS will in a greater extent ionize the sputtered target material. This allows for the deposition of high-quality films at lower pressures, making HiPIMS particularly useful for reactive deposition of thin films. Overall, HiPIMS offers improved deposition rates, better film quality, and greater control over film properties compared to traditional sputtering methods. HiPIMS leads to a high degree of N_2-ionization, allowing for great incorporation of elemental nitrogen in the films. Single crystalline $ZnSnN_2$ have been shown with an epitaxial growth on ZnO substrates by Olsen *et al.* [2] by using magnetron sputtering and HiPIMS.

3.1.5 RF-Sputtering

RF (radio frequency) sputtering is used when sputtering insulating or low conductive materials. When insulating or semi-insulating materials are sputtered, the ejection of secondary electrons, in addition to the atoms or molecules of the target material, creates a net positive charge on the target surface. This positive charge can build up over time and eventually become so strong that it extinguishes the plasma. To overcome the build-up of positive charge on the target surface when sputtering insulating materials, an alternating current (AC) signal is applied at radio frequencies. This AC signal accelerates positive ions towards the target when the signal is negative and negative electrons when the signal is positive. By doing so, it eliminates the surface charge build-up on the target. Since electrons have a much greater mobility than ions due to their lower mass, they contribute more to the electron flow through the anode than ions do at the cathode. This creates an asymmetry that leads to a negative self-bias in the RF sputtering system.

3.1.6 Reactive Sputtering

Reactive sputtering is a technique used to deposit compound films, such as oxides, nitrides, and carbides, which can be challenging to deposit by conventional sputtering techniques. Sputtering a target material with a reactive gas makes it possible to implement non-solid elements into the thin films, as the reactive gas reacts with the sputtered atoms or molecules to form a compound film on the substrate. The amount of gas that gets incorporated into the film is determined by factors such as the partial pressures of the gases, the characteristics of the plasma, and the sputtering power used within the chamber. To fabricate the $ZnSnGeN_2$ thin films in this thesis, the use of reactive sputtering was essential. Where Zn, Sn and Ge were co-sputtered as target materials, and N_2 was introduced in to the chamber as a reactive gas.

All depositions done in this study were performed by magnetron sputtering using the Polyteknik Flextura Cluster system at MiNaLab. This instrument includes two growth chambers, an annealing chamber, an analytical chamber, and a load-lock. The sputtering chamber contains five sputtering sources, including two DC soures, two RF sources and one HiPIMS, which can be used either individually or simultaneously. The Flexture system allows for both reactive and ordinary magnetron sputtering. The reactive sputtering processes in this work employed metallic targets of Zn, Sn, and Ge and N_2-gas for the deposition of $ZnSnGeN_2$. By regulating the different powers applied on the different targets, the composition ratios could be altered, spanning the whole range of the $ZnSn_xGe_{1-x}N_2$ alloy. Nitrogen of 99.9999% (6N) purity was used in the reactive atmosphere, the Ar gas used was 99.999% pure. The Flextura cluster also allows for substrate heating up to 1000°C, and since the system utilizes a load-lock, the deposition chamber has a low base pressure ($10^{-8} - 10^{-9}$ mBar), which is imperative when growing nitrides.

3.2 SEM EDS

Scanning Electron Microscopy (SEM) is used to create images of solid materials. By scanning the surface using a focused beam of high-energy electrons, it can give microscopic-scale information about the surface structure and composition of the material. Compared to an optical microscope, SEM provides a higher resolution, allowing for magnifications up to 200 000 times. The basic components of a SEM include an electron source, electron lenses, a sample chamber, a detector, and a computer system for image processing and analysis, see figure 3.2. The electron source typically consists of a tungsten filament or a field-emission cathode that produces a beam of electrons. The electron lenses focus the beam onto the sample, and the detector collects the signals emitted from the sample.

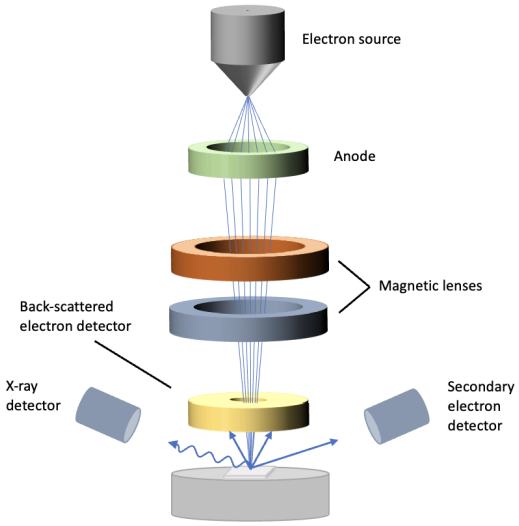

Figure 3.2: Schematics of a SEM setup. The x-ray detector is used for EDS measurments, while the back-scattered electron detector and secondary electron detector are utilized for creating surface images.

As the beam of focused electrons are directed to the surface of the sample, the electrons interact with the atoms on the surface of the sample and create signals that can be used to generate an image of the samples surface. The interaction creates backscattered electrons and secondary electrons. Backscattered electrons are primary and high-energy electrons which have been scattered back by atomic nuclei of the sample material. The intensity of the backscattered electrons depend on the mass of the nuclei in the collisions. These scattered electrons are then analyzed by a detector, making it possible to create a digital image of the surface. Heavier elements tend to produce more backscattering than lighter atoms, due to bigger nuclei. Since the heavier elements yield higher backscattering intensities, areas with heavier elements will appear brighter than areas with lighter elements in a SEM generated image. Secondary electrons are low-energy electrons that are emitted from the surface of the sample, and a product of ionization. If the energy of the primary electrons are high enough, it may transfer it's energy to bound electrons, where the atomic electrons can be ejected from it's orbital. Within the topmost 1-2 nm of the sample, the ejected electrons

can escape the sample and reach the detector. As only the secondary electrons from the top layer of the sample are detected, it is utilized for topographical examinations of the surface.

3.2.1 Energy Dispersive X-Ray Spectroscopy

Energy Dispersive X-Ray Spectroscopy (EDS) is a characterization technique that is often used in conjunction with (SEM) to identify the elemental composition of a sample. EDS is a non-destructive technique that analyzes the x-rays that are emitted from a sample when it is bombarded with high-energy electrons in an SEM. If the incident electrons have a high enough energy when they collide with the atoms in the sample, there will be an energy transfer which can excite atom electrons out of their shell, and leave empty states. The vacancies created by the ejected electrons are again filled by other electrons from higher energy levels. This jump into a lower energy shell releases excess energy in the form of a photon. Close to the nucleus, the energy difference between the electron shells correspond to photons in the x-ray range of the electromagnetic spectrum. A detector is used to measure the emitted x-ray and is able to characterize them by their wavelength.

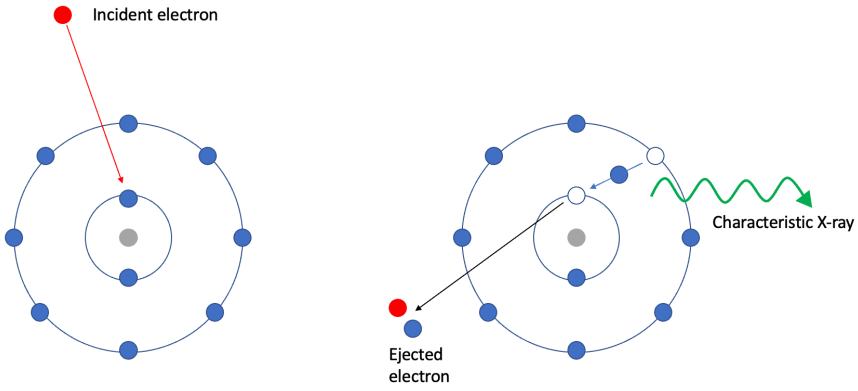

Figure 3.3: Schematics of characteristic x-ray emission as a result on an incident electron on an atom.

EDS detectors are positioned close to the sample in the SEM, collecting the x-rays that are emitted from the sample. Based on the many energy states electrons can occupy in an atom, there are several possible transitions that can occur. The energy of each x-ray is analyzed, and a spectrum of the x-ray energies, based on their wavelength, is generated. The spectrum can be used to identify the elements present in the sample, as each element has a characteristic set of x-ray energies. This x-ray profile is used to calculate the ratios of constituents in the sample with an precision between 0.1 - 0.5 *wt.%*. In a EDS measurement it is more challenging to distinguish between lighter elements, then heavy elements, as heavy elements tend to emit x-rays with higher energies than light elements. As the x-ray emission process involves the removal of an inner-shell electron from the atom, and heavy elements have more tightly bound inner-shell electrons than light elements, it takes more energy to remove them. Other factors that can affect the extracted results obtained in an EDS scan is the beam energy and current, the efficiency of the detectors, as well as the

sample composition.

In this work SEM EDS measurements were employed to determine the composition of the deposited thin films, where the stoichiometry and the varying cation composition are central factors and of major importance in growing alloys. A JSM-IT300 SEM stationed at MiNaLab equipped with a LaB_6 filament and a ThermoFischer UltraDry EDS detector were used. During the measurements a working distance between 11-12 mm and an acceleration voltage of 12 keV were applied. Films grown on conducting substrates, i.e., Si, were used in SEM EDS analysis to prevent surface charging.

3.3 X-Ray Diffraction

X-ray diffraction (XRD) is a widely used technique to probe the crystal structure of a material. The use of x-ray radiation is due to the fact that the wavelengths are approximately in the same magnitude as the distance between atoms, and therefore useful for characterizing structural properties of a material. Monochromatic Cu Kα radiation is typically used in XRD characterization, as this is filtered and only have one wavelength that contribute to diffraction. The incident x-rays are scattered by the atoms in the material, and the number of scattered photons, as well as the scattering angle, is measured by a detector. This method can give various information about the material, including the crystal quality, which phases that are present, lattice parameters and preferred orientation. XRD works on the principle of Braggs law, describing the relation between the incident x-ray beam and the diffracted beam from the crystal structure

$$2(d_{hkl})sin(\theta) = n\lambda \tag{3.3}$$

where d_{hkl} is the distance between the atomic planes, θ is the angle between the incident beam and the crystal structure, n is an integer and λ is the x-ray wavelength. The x-rays incident with an angle θ onto the crystal surface will be scattered with constructive interference when equation 3.3 is satisfied, that indicates that the difference in the beams path between the planes, $2dsin\theta$, is equal to a whole number of wavelengths. This is illustrated in figure 3.4.

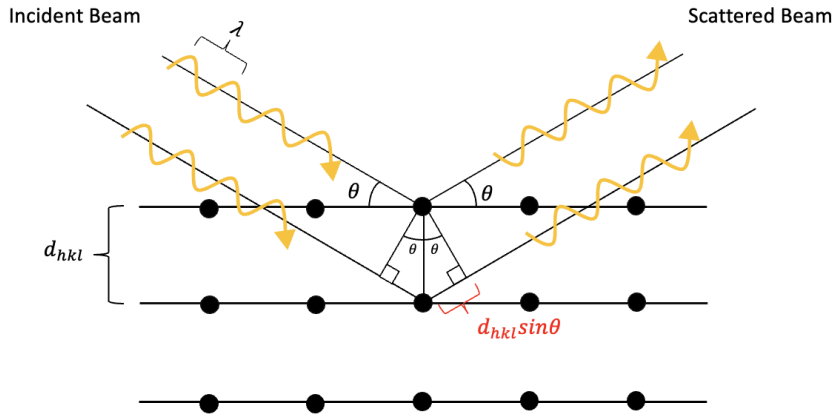

Figure 3.4: Bragg diffraction in a crystal structure illustrating the different path lengths between the atomic layers, d_{hkl}.

XRD is capable of extracting information about the crystal structure by analyzing the angles of diffraction. The peak position of diffraction as a function of 2θ is determined by the space between parallel planes, and the number of peaks observed is determined by the complexity of the materials structure, i.e., number of different phases and orientations. Single crystals, for example, only exhibit distinct peaks, e.g., (0002) and it's higher order replicas (0004), (0006), etc., since the entire crystal is grown in only one crystallographic direction. The intensity of the peaks is influenced by several factors, including plane density and electronic density of the atoms within the plane, with heavier atoms exhibiting more diffraction than lighter atoms.

Bragg's law can also be explained using vectors, where the incident and scattered beams are represented by the wave vectors $\mathbf{k}_0$ and $\mathbf{k}$, illustrated in figure 3.5b. The vector difference, $\mathbf{K} = \mathbf{k} - \mathbf{k}_0$, is called the scattering vector and changes accordingly to the wave vectors. If the incident and diffracted angles are identical, the scattering vector is normal to the sample, but as the angles are equally changed, the length of the scattering vector change accordingly. When the Bragg condition is satisfied, the length of the scattering vector $|\mathbf{K}|$ is the inverse of the lattice spacing, d_{hkl}, and also equal to the reciprocal lattice vector, $\mathbf{g}_{hkl}$. See figure 3.5*a*.

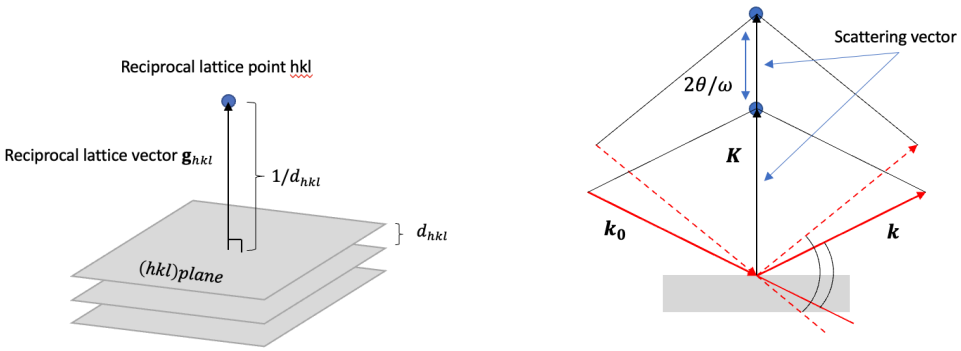

(a) (b)

Figure 3.5: (a) The reciprocal lattice vector and lattice point of a set of lattice planes (hkl) (b) Illustration of how the length of the scattering vector, $\mathbf{K}$, changes as a result of the incident, $\mathbf{k}_0$, and scattered, $\mathbf{k}$, wave vectors.

3.3.1 $2\theta - \omega$ Scan

XRD measurements usually detect the scattered x-ray intensity as a function of ω and/or 2θ, where $2\theta - \omega$ scans are widely used to study epitaxial films grown on single-crystal substrates. To register the Bragg reflections and their intensity, the x-ray source and detector are placed with an equal distance from the sample, forming a goniometric circle. The incident angle, ω, is defined between the source and the surface of the sample, and the diffracted angle, 2θ, is defined between the penetrated incident beam and the detector angle. An example of an experimental set up is illustrated in figure 3.6.

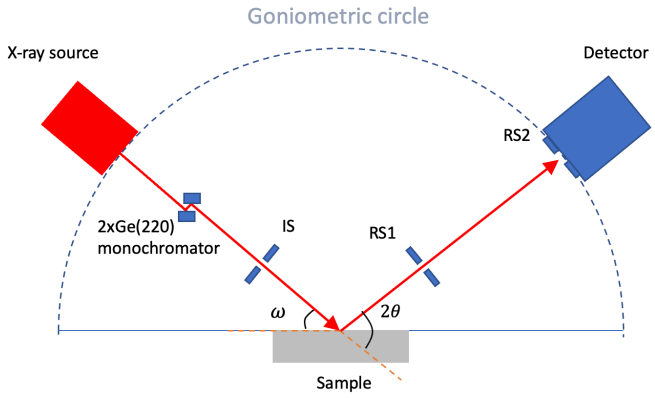

Figure 3.6: Illustration of experimental set up of a $2\theta - \omega$ scan.

In a $2\theta - \omega$ scan, the incident (ω) and diffracted (2θ) angle are kept equal and changed in a coupled manner. This type of measurement is a symmetrical scan, meaning that the scattering vector is perpendicular to the sample, so that $2\theta - \omega$ scan only measures crystallographic planes that are parallel to the surface of the sample. The distance between the planes (d_{hkl}) is completely decisive for the diffracting angle given by Braggs law, where the 2θ peak-position indicates a lattice parameter for the crystal structure. If a peak

shift to higher $2\theta - \omega$ values, it means the distance between the planes is reduced, and the oppositely, will a shift to a lower $2\theta - \omega$, indicate an increase in (d_{hkl}). Doping and annealing (relaxing the structure) are factors that can cause shifts in lattice parameters. In this way, a $2\theta - \omega$ scan is a powerful tool in analyzing both the presence of crystal phases, but also the alloy composition, which changes the lattice parameters, as well as strain in the material.

3.3.2 Rocking Curve Scan

Rocking curve, (ω), is a technique used to measure different crystallographic directions in the sample. ω-scans are conducted by fixing the detector at a $2\theta - \omega$-peak positions of the Bragg reflection, while rocking the incident beam around the peak position. This can also be thought of as tilting the sample slightly while measuring a Bragg peak. "Rocking" the sample around the ω-axis can be visualized in figure 3.7a.

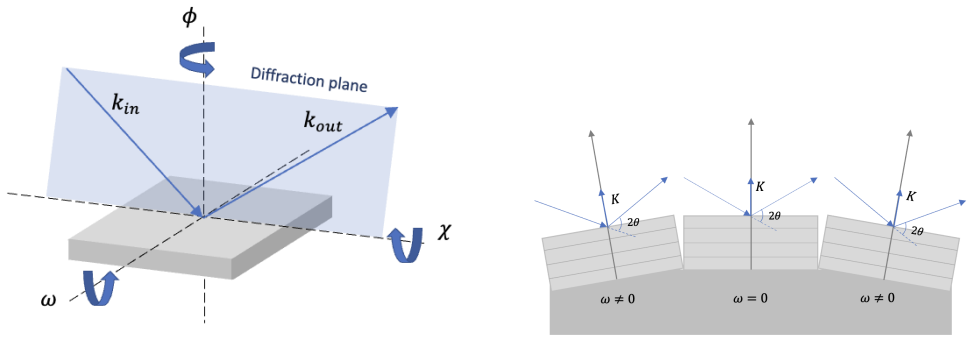

(a) (b)

Figure 3.7: (a) The samples rotational axis and diffraction plane of an incident and diffracted x-ray beam is visualized. Figure (b) shows the effect of tilting the sample around ω to measure asymmetrical planes in a crystal.

Since the detector is fixed at a specific Bragg reflection, only symmetrical planes parallel to the surface will be detected, when $\omega = 0$. By tilting the sample, crystallographic planes that are not parallel to the surface, called asymmetrical, will be perpendicular to the diffraction vector, and give rise to constructive interference when $\omega \neq 0$. The measurement returns the intensity as a function of tilt, and based on the measured diffraction intensities the distribution of tilt in the lattice planes can be determined. Rocking curves are the most important measure of crystalline quality. A narrow rocking curve, evaluated by the full-width at half-maximum (FWHM) indicates a high crystal quality. Dislocations in the films, in addition to difference in lattice constant, can cause tilts in the lattice planes. A broadening of a rocking curve peak is interpreted as a larger spread in the lattice plane tilt with respect to the surface normal, and can imply a higher concentration of dislocations in the material. Notably, the rocking curve scan broadness, FWHM, is connected to the distribution of lattice plane tilts with respect to the film normal, and can be used as an estimation of the dislocation density.

3.3.3 Phi Scan

In addition to analyzing the crystal phases, quality and alloy composition, XRD can also investigate the rotational symmetry of crystals by employing phi (ϕ) scans. For a ϕ scan, similarly to a ω-scan, the source and detector are held at a fixed Bragg peak of an intensity maximum. The sample stage is rotated 360° around the ϕ-axis, showed in figure 3.7a. A phi scan is done to determine the rotational symmetry of the crystal structure. As an example, the hexagonal structures have a six-fold rotational symmetry, and the diffraction would result in six distinct peaks, each separated by 60°.

Measurements done in this work is done with a Rigaku SmartLab 3 kW high-resolution X-ray Diffractometer, equipped with a Ge(440)x4 monochromator, CBO optics and D/teX Ultra 250 silicon strip detector.

3.4 Hall Effect Measurement

Hall effect measurement is a technique used to examine the electrical properties of semiconductors, specifically the carrier concentration, mobility and resistivity. The technique can be used to characterize both bulk and thin film materials and provides valuable information about the electrical behavior of the materials under different conditions, such as temperature. The Hall effect measurement setup consists of a sample, a current source to generate a current through the sample, a magnetic field source to apply a magnetic field perpendicular to the current and a voltmeter to measure the voltage across the sample perpendicular to both the current and the magnetic field.

3.4.1 The van der Pauw Methode

The van der Pauw method is a widely used technique for measuring the resistivity and Hall coefficient of materials with arbitrary shape. The requirements for using van der Pauw are, among other things, a sample that is much thinner than it's length and width, have a flat and uniform thickness, free of holes and isolated islands and contacts of negligible area. For a semiconductor the conductivity (σ) is inversely proportional with the resistivity (ρ)

$$\sigma = \frac{1}{\rho} = q(n\mu_n + p\mu_p) \tag{3.4}$$

where q is the elementary charge, n and p the concentration of electrons and holes, respectively, and μ_n and μ_p their corresponding mobilities. For a n-type semiconductor, where $n >> p$, the conductivity simplifies to $\sigma = \frac{1}{\rho} \approx q(n\mu_n)$, same as for a p-type with $p >> n$, the equation 3.4 modifies to $\sigma = \frac{1}{\rho} \approx q(p\mu_p)$.

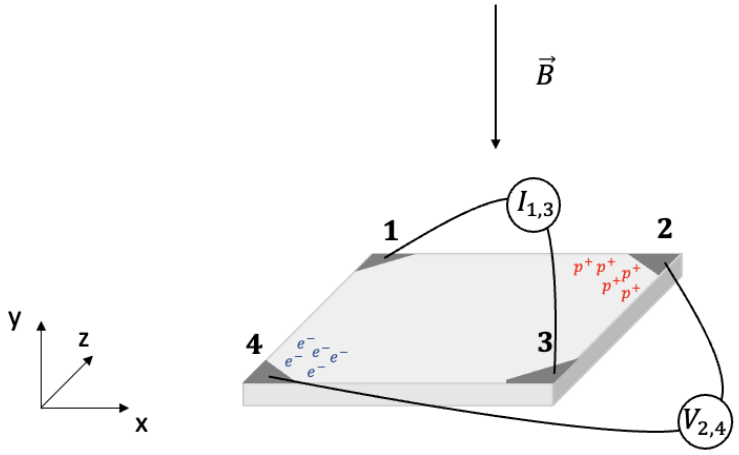

Figure 3.8: Illustration of a van der Pauw setup where a current is applied at contact 1 and extracted at contact 3. The voltage is measured between contact 2 and 4, while a magnetic field is applied in the negative y-direction.

For measuring the resistivity of a sample, four ohmic contacts labeled 1-4 are placed at each corner of the sample covering only a negligible area of the surface. A current is passed between two of the contacts, while the voltage drop is measured between the two remaining contacts. As shown as an example in figure 3.8, a current is applied to contact 1 and extracted from contact 3 while measuring the voltage drop between contacts 2 and 4. The resistance is found by dividing the measured voltage drop by the applied current

$$R_{13,24} = \frac{V_4 - V_2}{I_{13}} \tag{3.5}$$

By measuring the resistance for all equivalent geometries, and reversing the current, two average resistances can be calculated

$$R_1 = \frac{R_{13,24} + R_{24,13} + R_{31,42} + R_{42,31}}{4} \tag{3.6}$$

$$R_2 = \frac{R_{12,43} + R_{43,12} + R_{21,34} + R_{34,21}}{4} \tag{3.7}$$

The resistivity can then be determined by equation 3.8

$$\rho = \frac{\pi t}{ln(2)} \frac{R_1 + R_2}{2} F \tag{3.8}$$

where $F = 1$ for symmetric samples such as circles or squares. For samples that are not symmetric F needs to be taken into account when calculating the resistivity. Furthermore, with the use of Hall effect measurements, the resistivity can be used to determine the carrier concentration, and thereby also the mobility.

3.4.2 The Hall Effect

Current will travel in a straight line with a velocity, ν, when it is not exposed to any external influences. The electron velocity is related to the amount of applied current

$$\nu = \frac{I}{nAq} \tag{3.9}$$

where n is the electron concentration, while A is the cross section area of the sample and q is the elementary charge.

The Hall effect is a phenomenon that occurs when a magnetic field of magnitude B, is applied perpendicular to a current-carrying sample. The magnetic force acts on the electrons that are flowing through the sample with a force called the Lorentz force, $\vec{F_L} = q\nu \times \vec{B}$. $\vec{F_L}$ causes the electrons to deflect from their straight-line trajectory, in a direction perpendicular to both the current and the $\vec{B}$-field. This causes the electrons to accumulate on one side of the sample. Figure 3.8 illustrates an example, where the current is moving from contact 1 to contact 3, meaning electrons moving in the opposite direction, in addition to a magnetic field directed in a negative y-direction, so the electrons are deflected to contact 4. This accumulation of electrons produces an electric field, E, perpendicular to both the current and the magnetic field, in figure 3.8 pointing from a positive charge at contact 2 towards the negative charge at contact 4. The amount of accumulated electrons will increase until the force of the electric field, F_E, exactly balances the Lorenz force, i.e. when

$$F_E = F_L \tag{3.10}$$

By inserting equation 3.9 into equation 3.10, the electric field can be expressed as

$$E = \frac{IB}{nAq} \tag{3.11}$$

The voltage associated with this field is called the Hall voltage, V_H, and is directly proportional to the magnetic field strength, the current density and the carrier concentration of the material. V_H can be calculated by taking the integral of the electric field over the width of the sample.

$$V_H = \int_0^W EdW = WE = \frac{WIB}{qnA} = \frac{IB}{qnt} \tag{3.12}$$

where W is the width of the sample. From the Hall voltage the Hall coefficient, R_H, can be calculated

$$R_H = \frac{V_H t}{BI} \tag{3.13}$$

The sign of the Hall coefficient determine the polarity of the majority carriers, where a negative Hall coefficient indicates that electrons dominate and a positive value means that holes are in majority. The carrier concentration is then given by

$$n = \frac{r}{q|R_H|} \tag{3.14}$$

The Hall scattering factor, r, is a decisive quantity for the carrier concentration and also the drift mobility. Based on whether the scattering mechanisms limiting the mobility are independent of energy. For Hall measurements it is often assumed to be 1 [39].

By repeating the resistivity and Hall effect measurements for a range of temperatures one can extract information about donor or acceptor levels responsible for the carrier concentrations as well as the mechanisms limiting the mobility of the sample. It is commonly accepted that ionized impurities and acoustic phonons are the main limitations of mobility in many materials. The temperature dependence of the mobility limited by these two scattering mechanisms is found to be $\mu_{II} = T^{3/2}$ and $\mu_P = T^{-3/2}$ [11].

For the Hall measurements preformed in this work, a Lakeshore 7604 Hall effect measurement system situated at MiNaLab was used. Both room temperature and temperature dependent measurements, in the range of 20-300 K, was conducted in a He atmosphere and an applied magnetic field strength of 1.0 T.

3.5 UV-VIS Spectroscopy

A materials optical properties are determined by the way in which electromagnetic radiation interacts with the material. The technique, ultraviolet-visible (UV-VIS) spectroscopy is based on directing light with varying wavelengths onto a sample, and observe how the light interact with the material. The wavelength, i.e., the energy, of the incident light beam is varied from the ultraviolet (UV) where $\lambda \approx$ 180-380 nm, through the visible part of the spectrum with $\lambda \approx$ 380-750 nm to the infrared region with $\lambda \gtrsim 750$ nm. Light waves interact in four different ways with semiconductors; transmission, reflection, absorption and scattering. If the energy of the incident light is lower than the bandgap of the material, ideally no light would be absorbed, and most of it would be transmitted. Oppositely, will light with energy higher than the bandgap be absorbed.

Beer-Lamberts law relates the intensities of incident light onto a sample, to transmitted light through the following equation, assuming no scattering.

$$I_t = I_0 e^{-\alpha(\lambda)d} \tag{3.15}$$

where I_t is the intensity of the transmitted light and I_0 is the intensity of the incoming light. $\alpha(\lambda)$ is the wavelength dependent absorption coefficient, and d is the thickness of the sample. During a transmission measurement the detector measures the amount of transmitted light i.e., the amount of light that goes through the sample. In the same way as a reflection measurement measures the amount of light that is reflected by the sample. Figure 3.9 shows a transmission spectrum, where the measured transmission is plotted as a function of wavelength. These two types of measurements, as well as equation 3.16 can

be used to calculate the absorption coefficient, α, which is an important factor in further estimating the bandgap of the material. The transmission can be defined as

$$T = \frac{(1-2)^2 e^{-\alpha d}}{1-2^2 e^{-2\alpha d}} \approx (1-R)^2 e^{-\alpha d} \tag{3.16}$$

where T is the percentage of transmitted light, R is the percentage of reflected light and d is the thickness of the thin film. The absorption coefficient, α, is defined as the fraction of the incident flux that is neither transmitted or reflected, and demonstrated in figure 3.10.

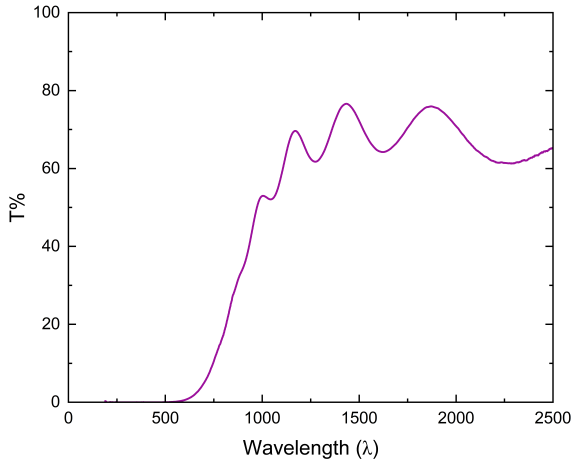

Figure 3.9: shows raw data from a transmittance measurement, where the transmission is plottet as a function of the varying wavelength of the incident light.

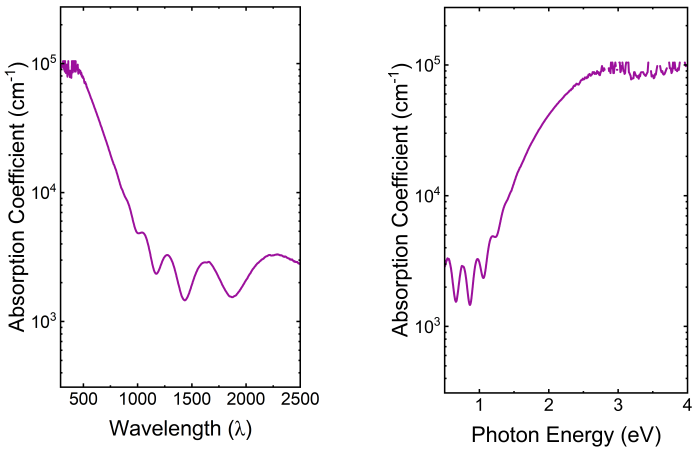

(a) (b)

Figure 3.10: shows the calculated absorption coefficient from the transmission data as a function of (a) wavelength and (b) photon energy.

3.5.1 Tauc Analysis

Tauc plots are commonly used to estimate the optical bandgap for semiconductors. The Tauc method is based on the assumption that the absorption coefficient can be expressed

by the following equation

$$[\alpha(E)h\nu]^{1/r} = c(h\nu - E_g) \tag{3.17}$$

where α(E) is the absorption coefficient, $h\nu$ is the photon energy, c is a structure dependent constant, E_g is the bandgap and r is a number that depends on the type of absorption, where $r = 2$ for indirect allowed transitions and $r = 1/2$ for direct allowed transitions. In order to estimate the bandgap using Tauc plot analysis, $(h\nu\alpha)^{1/r}$ is plotted as a function of the photon energy, $h\nu$. Figure 3.11a shows a Tauc plot of a direct allowed transition, and how α rapidly drops to zero in the region close to the bandgap of the material. The bandgap can be estimated by linear extrapolation, where the intersect at the energy-axis with the extrapolation is interpreted as the material bandgap. The deviation from the extrapolation of the linear region is known as an absorption tail and depends on the degree of disorder and defects [40].

3.5.2 α - Analysis

Zanatta *et al.* explained in an article [41] that the optical absorption coefficient of an electron being excited from the valence band to the conduction band, is exposed to the transition rate

$$W_{VB\to CB} = \frac{2\pi}{\hbar}|M|^2 g(E) \tag{3.18}$$

where M represents the (coupling) transition matrix element and $g(E)$ is the (joint electron-hole) density of states. For a semiconductor with a direct bandgap, there is no change in the momentum, $\vec{k}(\vec{k_f} \approx \vec{k_i})$, and the absorption coefficient α(E) is expected to behave like:

$$\alpha_{dir}(E < E_{gap}) = 0, \tag{3.19}$$

and

$$\alpha_{dir}(E \geq E_{gap}) \propto (E - E_{gap})^{1/2} \tag{3.20}$$

In such a case, the semiconductor is said to exhibit an optical direct bandgap and it's E_{gap} value can be determined by linear extrapolation the absorption coefficient to the power of two, α^2, in a "α^2 versus E" plot, see figure 3.11b. Similar to Tauc analyse, α^2 plot provide reasonable estimates of E_g [41]. In the case of indirect optical transitions a photon and a phonon is required to excite an electron. As a consequence, the transition rates in indirect bandgap semiconductors are generally smaller than those in the direct bandgaps. The optical absorption coefficient for an indirect semiconductor can be written:

$$\alpha_{ind}(E < E_{gap}) = 0, \tag{3.21}$$

and

$$\alpha_{ind}(E \geq E_{gap}) \propto (E \pm \hbar\Omega - E_{gap})^2, \tag{3.22}$$

where $\hbar\Omega$ denotes the energy of a photon being emitted or absorbed, and can in most cases be neglected. Indirect E_g values can be obtained from the intersect at the energy-axis with the extrapolation of the linear region of $\alpha^{1/2}$.

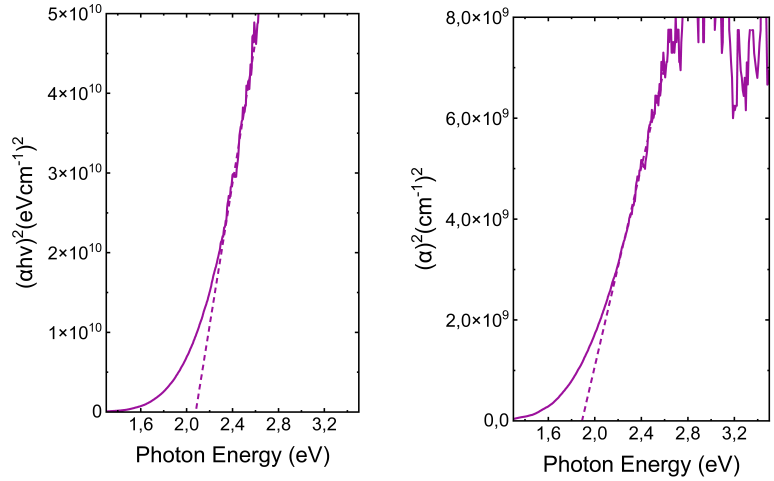

(a) (b)

Figure 3.11: Example of bandgap estimation with the use of (a) Tauc- and (b) α^2 plot. The intersection of the dashed lines with the horizontal energy-axis indicates the bandgap value in both cases.

In this work both bandgap estimation methods have been used. Since both are estimations, the difference in estimated E_g represents the uncertainty. A Shimadzu SolidSpe-3700 DUV spectrophotometer, equipped with both a Deuterium and Tungsten lamp, was used for all UV-VIS measurements. Transmission and reflection measurements was the basis of the estimated absorption coefficient, α(E), and bandgaps. The wavelengths were varied between 190-2500 nm with a step size of 1 nm.

3.6 Secondary Ion Mass Spectrometry (SIMS)

Secondary Ion Mass Spectrometry (SIMS) is a high-resolution technique used to analyze the chemical composition of materials, detecting trace amounts of elements and isotopes with a sensitivity down to parts per billion and depth resolution down to 2 nm. The technique involves bombarding a solid sample with a beam of high-energy primary ions to generate and analyze the secondary ions emitted from the surface. SIMS is mainly used for measuring small concentrations in a given matrix and has three measurement modes: mass spectra, depth profiling, and ion imaging. All methods use a primary ion beam, usually O_2^+- or Ce^+-ions to enhance ionization. The ions incident on the sample, bombarding the surface, causing atoms and ionized species (secondary ions, neutral atoms, molecules) to be sputtered off, making SIMS a destructive method.

SIMS are often divided into two main types; static SIMS and dynamic SIMS. Dynamic

SIMS use high ion flux, bombarding the sample with a continuous high-intensity primary ion beam, to investigate the composition as a function of depth. On the other hand, static SIMS uses a low-intensity pulsed ion beam to analyze the sample surface. Instruments are also usually classified into Quadropole, Time-of-Flight and Magnetic sector by the type of mass spectrometer. The instrument used in this work detect the secondary ions is by magnetic sector, where secondary ions first go through an electrostatic sector analyzer, using two curved metal plates at different potential for energy filtering. After exiting the electrostatic sector analyzer, secondary ions enters a magnetic sector analyzer, where a perpendicular magnetic field causes the pathway of the ions to bend. The curvature of the ions pathway is mass dependent, thus the magnetic sector analyzer acts as a mass filter. The magnetic field is then adjusted so that only the desired ions are passed through a slit, where they are registered by a detector. While a depth profile is formed by keeping the magnetic field constant, allowing only a certain element to pass, while the primary ions sputter through the thickness of the film. The detector measures intensity as a function of time, which again can be converted into concentration into concentration versus depth using standards and measuring creter depth.

In this work SIMS measurements have been done by a Cameca IMS 7f magnetic sector SIMS with a primary beam of 10 keV O_2^+-ions. Prof. Lasse Vines and PhD student Ylva K. Hommedal have conducted SIMS measurements used in parts of this study.

3.7 Fourier-transform infrared spectroscopy (FTIR)

In FTIR (Fourier Transform Infrared) spectroscopy, a beam of infrared light is passed through a sample, and the amount of light absorbed by the sample is measured as a function of the frequency of the infrared radiation. The resulting spectrum can provide information about the chemical bonds present in the sample, as well as investigate absorption arising from impurities. FTIR spectroscopy is based on the principle of Fourier transformation, which is used to convert the time-domain signal into the frequency domain. In FTIR, the sample is exposed to a wide range of infrared radiation frequencies, and the resulting signal is collected using a detector. The signal is then Fourier transformed to produce a spectrum that contains information about the vibrational modes of the chemical bonds in the sample. The FTIR spectrum is typically displayed as a plot of intensity versus frequency or wavelength. The peaks in the spectrum correspond to the different types of chemical bonds present in the sample. By comparing the spectrum of an unknown sample to a library of known spectra, the identity and composition of the sample can be determined. The FTIR instrument can also be used to conduct transmission measurements in the infrared region, i.e., extending the range measurable by UV-Vis spectrometry. The transmittance (and calculated α) in the infrared region, can give insight in the absorption of low-energy photons, relevant for e.g., semiconductors with high carrier concentrations where free-carrier absorption might be relevant.

Dr. Eirini G. Zacharaki have been the one doing the FTIR measurements utilized in

this thesis. The UiO MiNaLab is equipped with a Bruker IFS 125HR Fourier Transform spectrometer that measures IR light transmitted through a material. The IFS 125HR can achieve a spectral resolution of up to 0.0063 cm^{-1}.

Chapter 4

Results and Discussion

This chapter is devoted to the results obtained from this work, with the motivation of developing a new earth abundant solar cell material for tandem solar cells. $ZnSn_xGe_{1-x}N_2$ alloys are deposited with the aim of combining the lower carrier concentration of $ZnGeN_2$ and the optical bandgap of $ZnSnN_2$, both desirable for solar cell applications. With a prior knowledge that $ZnSnN_2$ and $ZnGeN_2$ are naturally occurring n-type materials, n-type conductivity is also to be expected for the $ZnSn_xGe_{1-x}N_2$ alloy. The carrier concentration of $ZnSnN_2$ has frequently been observed in the range of 10^{21} cm^{-3}, indicating a carrier concentration at or above degenerate doping level [7, 2], while the lower carrier concentration of $ZnGeN_2$ is more suitable for solar cells. In contrast, the bandgap of $ZnSnN_2$ ($\sim$1.7 eV) [2] is more suitable for tandem applications compared to $ZnGeN_2$, which has a larger bandgap size of $\sim$3.1 eV [4]. Hence, the $ZnSn_xGe_{1-x}N_2$ alloy series are investigated to determine the alloys ability to tune the carrier density and bandgap as a function of composition.

In this study, two $ZnSn_xGe_{1-x}N_2$ alloy series were deposited and further explored. Along with a complete stoichiometric series, a full non-stoichiometric series was grown, not previously reported for this alloy. The inspiration for this approach came from Fioretti's work on pure $ZnSnN_2$, where it was found that by adjusting the cation off-stoichiometry, the carrier concentration of as-grown $ZnSnN_2$ could be lowered to 1.8×10^{18} cm^{-3} [7]. In both series a full composition range where attempted grown. The ambition of this work was to understand and control electrical and optical properties of this novel class of materials, and by that obtain a tunable bandgap and carrier concentration as a function of alloy composition.

4.1 Sample Preparation

All thin films included in this work were grown by reactive co-sputtering. This growth method provides high flexibility to tailor the desired compositions of the various thin films. Previous work on $ZnSnN_2$ has provided knowledge about the process developments and deposition parameters, something this work have benefited from and developed further. Using a Flextura cluster system equipped with HiPIMS and RF sources, the films were grown with Ar and N_2 as inert and reactive gases, respectively. The Zn target was positioned

at the HiPIMS source, while Sn and Ge targets were sputtered with RF sources. HiPIMS has proven to be a beneficial method for growing nitrides as it yields a higher ionization of the N_2 reactive gas, and was therefore utilized in this work.

Substantial process development steps were carried out to optimize the concentration ratios, especially with regard to balancing the ratio of the three cations Zn, Sn and Ge. Variables like the applied target powers, process pressure, N_2 flow, deposition time and substrate temperature are all factors that affect the quality and the composition of the thin films. A majority of these parameters were carefully tuned to span the entire stoichiometric and non-stoichiometric alloy composition range. To cover the full range of $ZnSn_xGe_{1-x}N_2$, containing $0 \leq x \leq 1$, the Sn/Ge ratio were tuned by regulating the applied Sn and Ge target powers. Additionally, for the deposition of the non-stoichiometric alloy, the HiPIMS target power (Zn) were increased in comparison to the stoichiometric alloy. By increasing the Zn power, while keeping the same recipe for the Sn/Ge ratio, a full Zn-rich non-stoichiometric $ZnSn_xGe_{1-x}N_2$ alloy series were made, with the exception of $ZnGeN_2$.

For all depositions the HiPIMS frequency were held constant at 1400 Hz, likewise were the process pressure and N_2 flow keep constant at 2.60×10^{-3} mbar and 20 sccm, respectively. The two alloy series were grown with the same deposition parameters, except for the Zn-ratio, which were increased for the non-stoichiometric alloy series. The final deposition parameters for both the alloys are showed in table 4.1. The optimal growth temperature for $ZnSnN_2$ is 350°C [7], while $ZnGeN_2$ exhibit a higher optimal growth temperature at $\sim$ 500°C [26]. The growth temperature was therefore increased from 350°C to 500°C through the alloys going from $ZnSnN_2$ to $ZnGeN_2$, to ensure high crystalline quality.

Table 4.1: Deposition parameters of the stoichiometric and non-stoichiometric alloy series.

Sample Name	HiPIMS (Zn) Power [W]	RF1 (Sn) Power [W]	RF2 (Ge) Power [W]	Deposition Time [min]	Substrate Temperature [C°]
Stoichiometric Alloy Samples					
$ZnGeN_2$	40	0	60	300	500
A	40	15	46	300	400
B	45	17	39	300	400
C	45	19	37	300	400
D	45	29	39	300	350
E	45	27	29	300	350
F	45	31	25	300	350
G	45	35	21	300	350
H	45	39	17	300	350
$ZnSnN_2$	45	46	0	300	350
Non-stoichiometric Alloy Samples					
A2	65	15	46	300	400
B2	65	17	39	300	400
C2	65	19	37	300	400
D2	65	29	39	270	350
E2	65	27	29	300	350
G2	65	35	21	270	350
H2	65	39	17	270	350
I2 ($ZnSnN_2$)	65	46	0	270	350

The thin films were grown on various substrate materials. During the development process p-Si and sapphire, c-Al_2O_3, were used based on the fact that they are inexpensive and readily available. However, they exhibit a large lattice mismatch and are not optimal for epitaxial growth. The Si substrate made it possible to investigate the composition of the thin films with SEM EDS, since it is electrical conductive. One the other hand, the growth on c-Al_2O_3, which is an insulating material, was advantageous for investigating electrical properties preformed with Hall effect measurements. GaN substrates were chosen to study the structural properties, as GaN have been reported to have a lattice mismatch <5% compared to $ZnSnN_2$ [5]. Additionally, GaN is most stable in the wurtzite structure, which is also the structure expected for $ZnSnN_2$ and $ZnGeN_2$.

As a final result a full stoichiometric and non-stoichiometric alloy series were grown on phosphorus (P) implanted ZnO. ZnO also crystallizes in the wurtzite structure, and were chosen since the lattice closely match that of $ZnSnN_2$, with a lattice mismatch of $\sim 4.2\%$ [19]. Therefore, ZnO represents the best material for epitaxial growth of $ZnSnGeN_2$. Prior to the thin film depositions, the ZnO substrates were implanted with P, followed by post-annealing to repair structural damages and activate the compensating acceptors after implantation. The P-doping of the ZnO substrate was done for the purpose of inserting an isolating layer between the thin films and the substrate, due to the fact that the ZnO substrates where initially n-type conductive, and therefore enable reliable electrical measurements.

Table 4.2: Lattice mismatch compared to $ZnSnN_2$.

Substrate material	Lattice mismatch
Si	
c-Al_2O_3	
GaN	$< 5\%$ [5]
ZnO	$\sim 4.2\%$ [19]

For a material to work in a tandem solar cell, the structural, electrical and optical properties are of great importance. The stoichiometric and non-stoichiometric alloy series of $ZnSn_xGe_{1-x}N_2$ have therefore been investigated with the characterization methods explained in chapter 4.

4.2 Annealing series of $ZnSnN_2$

The growth of $ZnSnN_2$ is to a large extend based on the previous work reported by Olsen *et al.* [2], who were able to optimize the growth conditions for $ZnSnN_2$, and showed epitaxial growth on ZnO substrates with a growth temperature of 350°C. The initial phase of this research was therefore to conduct an annealing series of $ZnSnN_2$ deposited with the same deposition parameters as Olsen *et al.* [2], to further investigate the material and the effect of post-growth annealing temperature. The crystal structure was examined with XRD measurements, comparing an as-grown thin film with two samples annealed for an hour at 400°C and 450°C.

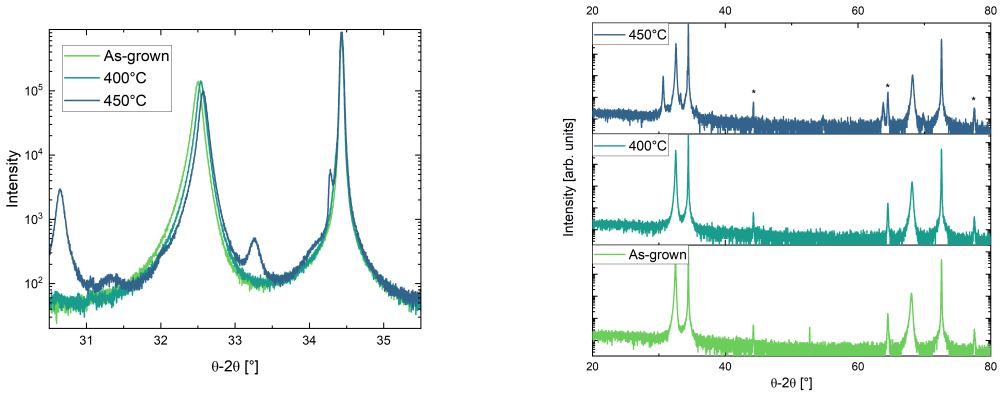

(a) (b)

Figure 4.1: X-ray diffraction $\theta - 2\theta$ measurements (a) highlighting the (0002) peaks and (b) showing a wide-scan.

Figure 4.1 provides XRD $\theta - 2\theta$ scans examining the effect of annealing on the crystal structure of $ZnSnN_2$, where the intensity of the Bragg diffraction is shown on the vertical axis as a function of the $\theta - 2\theta$ angle. A wide scan, covering a range from 20° to 80° is shown in figure 4.1b. The wide-scan clearly shows peaks of higher intensity, indicating crystal planes in the material. The peak located at ∼32.5° is identified as the (0002) peak

for $ZnSnN_2$, while the (0002) from ZnO is located at ∼34.5°. Additionally are, their (0004) replicas found at ∼68.0° and ∼72.6°. A more detailed scan of the (0002) planes are displayed in figure 4.1a, showing that a post-grown annealing of 450°C causes new diffraction peaks, that the as-grown and the one annealed at 400°C do not exhibit. New Bragg diffraction peaks clearly indicate the presence of other planes than the (0002) plane, specifically the (110) and (101) with diffraction peaks found at ∼30.6° and ∼33.3°, respectively [42]. Hence, additional crystal directions, meaning the film converts to polycrystalline, are observed at the annealing temperature of 450°C.

4.3 Growth temperature and post-growth annealing of $ZnGeN_2$

For a slightly more detailed examination of $ZnGeN_2$, four sputtered thin films were exposed to different growth temperatures and in-situ post-growth annealing steps. As $ZnGeN_2$ require a higher optimal growth temperature compared to $ZnSnN_2$ [26, 2], thus, $ZnGeN_2$ were grown on 350°C and 500°C, whereas two were grown on 350°C, followed by in-situ post-growth annealing at 650°C and 750°C.

XRD $2\theta-\omega$ scans were performed on the $ZnGeN_2$ thin films to study the effect of temperature on the crystal structure. Wide scans were initially conducted, as shown in Figure 4.2a, but no indications of the (0002) thin film peak were observed for any of the films. The observed peak located at ∼53° could possibly be explained by Zn_3N_2, which is expected to have a (440) peak at 52.924°. The diffraction peaks for ZnO and $ZnGeN_2$ are very close to each other, so the receiving slit used for all other scans (1.1 mm) was too wide to resolve the two peaks. Therefore, new scans were conducted with a smaller receiving slit of 0.1 mm, which resulted in the scans shown in Figure 4.2b. Figure 4.2b shows that the substrate has a distinct peak at it's normal diffraction position. For the thin film grown at 350°C, the XRD pattern shows two peaks, indicating the presence of two crystallographic phases, which we believe corresponds to (0002) ZnO. The intensity of both peaks are lower than the two other scans, for which the reason is unclear. $ZnGeN_2$ grown at 500°C shows a wider peak at the same diffracting angle, which we in combination with no evidence of other $ZnGeN_2$ related peaks in the wide scan, interpret as the presence of a $ZnGeN_2$ thin film with a very similar lattice constant as that of ZnO. Based on this, as well as the reported results from Tellekamp *et al.* [26], which showed optimal growth at ∼ 500°C, the $ZnGeN_2$ thin films grown at this temperature were selected for further investigation in this study.

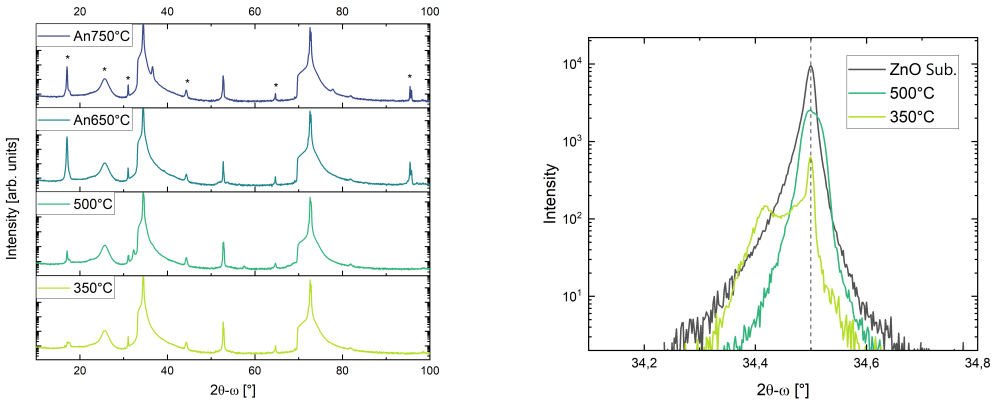

(a) (b)

Figure 4.2: (a) X-ray diffraction $2\theta - \omega$ measurements of the four $ZnGeN_2$ thin films grown and post-growth annealed at different temperatures (b) $2\theta - \omega$ measurements highlighting the (0002) peak.

Hall measurements were also preformed on the various $ZnGeN_2$ thin films, to investigate if the growth temperature or post-growth annealing affected the electrical properties of the thin films, see table 4.3. At room temperature the different $ZnGeN_2$ thin films exhibited very similar electrical properties, as shown in Table 4.3. The thin film grown on 350°C without any annealing had a carrier concentration of 1.02×10^{18} cm^{-3}, and a mobility of 177.2 $cm^2/(Vs)$, while the thin film grown on 500°C showed a carrier concentration of 1.62×10^{18} cm^{-3} and mobility of 161.7 $cm^2/(Vs)$. For the post-grown annealed samples, the one post-annealed at 650°C had a carrier density of 1.18×10^{18} cm^{-3}, and a mobility of 160.4 $cm^2/(Vs)$, and the sample annealed at 750°C exhibited a carrier concentration of 7.78×10^{18} cm^{-3} and mobility 162.6 $cm^2/(Vs)$. All of the thin films exhibit high mobility and carrier concentrations significantly lower than $ZnSnN_2$, as expected for $ZnGeN_2$.

Table 4.3: Carrier concentration and mobility for $ZnGeN_2$ at different growth temperature and post growth annealing.

Growth temperature [°C]	Post growth annealing [°C]	Carrier concentration [cm^{-3}]	Mobility [$cm^2/(Vs)$]
350		1.02×10^{18}	177.2
500		1.62×10^{18}	161.7
350	650	1.18×10^{18}	160.4
350	750	7.78×10^{18}	162.6

Figure 4.3 displays SEM surface scans of the $ZnGeN_2$ thin film grown at 500°C. These scans were performed to obtain a visualization of the sample surface and not for a more extensive analysis. Both scans were conducted at 20 kV with magnifications of x9,500 and x100,000, respectively. The left image show the presence of dust particles on the surface, and the grains in the right photo indicate that the growth was not a single crystal growth.

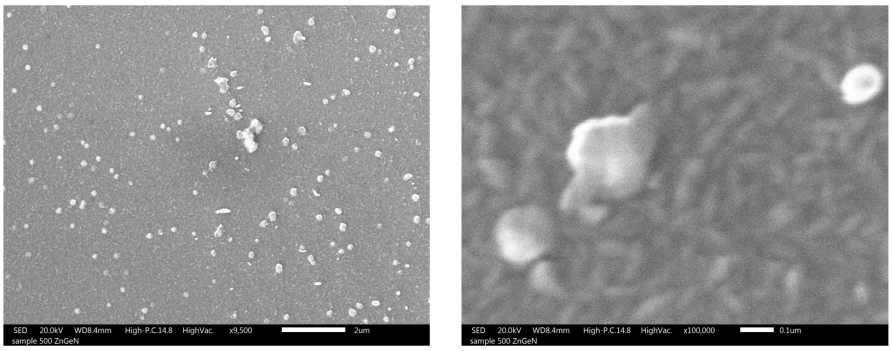

Figure 4.3: SEM surface scans of $ZnGeN_2$ with growth temperature 500°C.

4.4 Stoichiometric $ZnSn_xGe_{1-x}N_2$ Alloy

A stoichiometric alloy series with ternary compounds $ZnSnN_2$ and $ZnGeN_2$ were grown with the purpose of an experimental investigation of the alloy structure and optoelectrical properties. The thin films were grown on P-implanted ZnO, and labeled A-H, with A being the most Ge-rich sample, and H being the most Sn-rich, while the ternary compounds where labeled $ZnGeN_2$ and $ZnSnN_2$. The growth parameters of the deposited thin films are described in table 4.1, and resulting compositions are presented in table 4.4. The elemental composition of the cation stoichiometry and alloy composition in table 4.4 are based on SEM EDS, performed with point ID measurements, since it is well known that SEM EDS yields relatively large uncertainties in the elemental quantification, especially for elements such as nitrogen, the EDS results were used to estimate the cation ratios, as presented in Table 4.4, and not report elemental concentrations. The atomic composition were measured at multiple points on each of the thin films, to potentially detect compositional differences. SEM EDS spectral imaging were also utilized to examine the homogeneity of the thin films, where the thin films showed high degree of uniformity, with no indications of elemental gradients or clustering, see figure 4.4. The thickness of the deposited thin films were measured with the use of a stylus profilometer, resulting in a range of 500 nm - 1 μm depending on the deposition parameters.

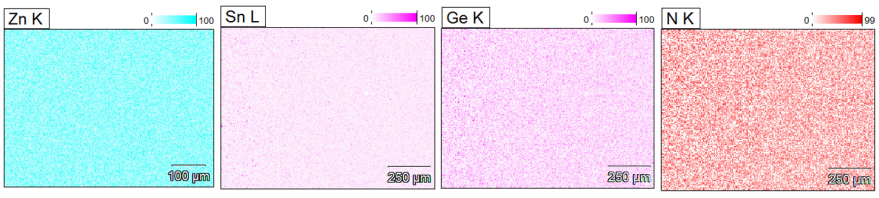

Figure 4.4: SEM EDS spectral imaging on sample C, showing a uniform composition of the four atomic elements.

Table 4.4: Composition of the stoichiometric alloy samples. The cation stoichiometry and alloy composition are extracted with SEM EDS, while the thickness was obtained by stylus profilometer measurements.

Stoichiometric Alloy Samples			
Sample name	Cation stoichiometry (II/II+IV)	Alloy composition Sn_xGe_{1-x}	Thickness [nm]
$ZnGeN_2$	0.50	0.00	583.6
A	0.49	0.23	532.4
B	0.51	0.31	631.9
C	0.50	0.37	637.4
D	0.52	0.52	1091.5
E	0.52	0.56	734.9
F	0.52	0.68	674.7
G	0.52	0.78	1030.5
H	0.53	0.84	1175.5
$ZnSnN_2$	0.49	1.00	909.2

4.4.1 Structural Properties

For the structural properties investigated with XRD measurements, $ZnSnN_2$ and sample D are absent from the results, as they were passed on to another master student for further TEM studies.

XRD measurements were used to examine the structural properties of the alloys. Figure 4.5 presents XRD $2\theta-\omega$ scans of the stoichiometric alloy series with varying compositions grown on (0001) P:ZnO substrates, where the intensity of diffraction is plotted as a function of the diffracting angle. For all samples, A-H, four distinctive peaks are observed, in addition to several peaks of lower intensity. The four diffraction peaks exhibiting the highest intensities are, similarly to figure 4.1b, identified to originate from the (0002) and (0004) wurtzite planes of the ZnO substrate and $ZnSn_xGe_{1-x}N_2$ thin films. The (0002) $ZnSn_xGe_{1-x}N_2$ plane slightly shifts position between $\sim 33.95°$ (sample A) and $\sim 32.87°$ (sample H). While the replica, (0004) $ZnSn_xGe_{1-x}N_2$ varies in the range of $\sim 72.76°$ (sample A) to $\sim 69.89°$ (sample H). The diffraction peaks marked with (*) are caused by the substrate or surroundings, and can therefore be disregarded when analyzing the structural quality of the alloy. The diffraction peaks highlighted with dotted lines are not fully identified. The diffraction located at $\sim 13.8°$ (dotted line) are only visible for the Ge-rich part of the alloy, and it is therefore reasonable to argue that these indicate Ge-phases. Cross-referenced with databases Ge_3N_4 is the only one found in close proximity with a diffracting angle at 12.563° for the (100) plane. Additionally, for some of the samples a diffraction peak at $\sim 53°$ is observed, which could possibly be explained by Zn_3N_2, which is expected to have a (440) peak at 52.924°, but this is not investigated further.

It appears not to be an epitaxial relationship between the grown layer of $ZnSn_xGe_{1-x}N_2$ and ZnO substrate, due to the presence of other thin film related diffraction peaks then the (0002) ZnO, (0002) $ZnSnN_2$ and their (0004) replicas, clearly shown in figure 4.5. However,

it is clear that the films have a predominant growth direction that is similar to that of the substrate, and that the deposited alloys possess a decent crystal quality.

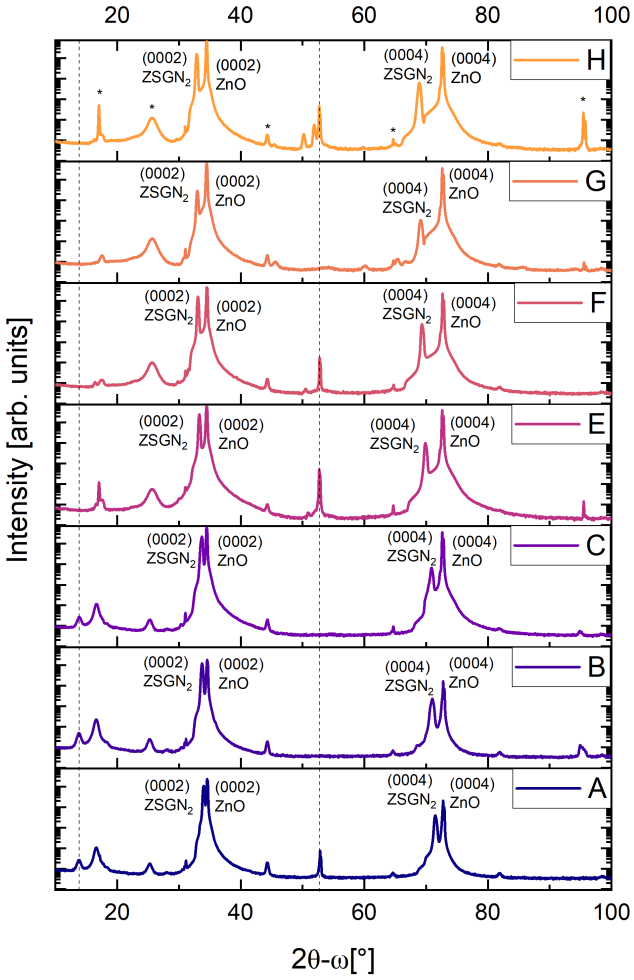

Figure 4.5: Wide x-ray diffraction scans of the stoichiometric alloys.

Figure 4.6a shows a more detailed $2\theta - \omega$ scan focusing on the most intense (0002) reflection. One can observe that the angle of the (0002) $ZnSn_xGe_{1-x}N_2$ peak shifts throughout the alloy as a function of alloy composition. The most Sn-rich sample, H, diffracts at a lower angle $\sim 32.87°$, followed by an almost monotonous increase in the peak positions as a result of the increased Ge-content, culminating at $\sim 33.95°$ for sample A. The $ZnSn_xGe_{1-x}N_2$ exhibits a near-linear relationship between it's c-lattice parameter and composition, indicating that it closely approximates Vegard's law [43], see figures 4.6a and 4.6b. The (0002) alloy peak shifts between the dotted lines representing the (0002) diffraction peak of $ZnSnN_2$ at $\sim 32.4°$ [2] and $ZnGeN_2$ ~ 34.4 [26]. The fact that none of the alloys have peaks at the $2\theta - \omega$ positions of $ZnSnN_2$ or $ZnGeN_2$ suggests that the $ZnSn_xGe_{1-x}N_2$ alloy have a continuous variable composition and is, indeed, a random alloy and not a combination of the $ZnSnN_2$ and $ZnGeN_2$ phases. Except for sample C, which shows the presence of a shoulder peak, only one prominent peak is observed in the $2\theta - \omega$ range of the (0002)

reflection. This observation supports the theory that phase separation is not a significant issue in this material.

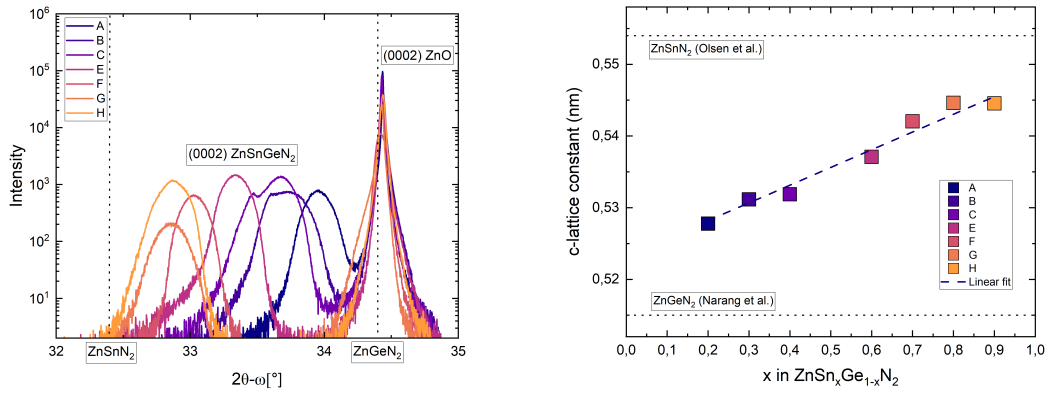

(a) (b)

Figure 4.6: (a) $2\theta - \omega$ scan showing a shift in the (0002) peak position for the stoichiometric alloys. The marked lines indicates the peak position for $ZnSnN_2$ and $ZnGeN_2$. (b) c-lattice constants for the alloys. Dotted lines indicates the c-lattice constant for $ZnSnN_2$ and $ZnGeN_2$ calculated from Olsen *et al.* [2] and Narang *et al.* [4], following Vegards law.

The "continuous" nature of the alloys is also illustrated by a linear relationship between the c-lattice constants in figure 4.6b. The interplanar atomic distance d_{hkl} corresponds to the c-lattice constant for growth in the same direction as the (0001)-cut ZnO substrate. The linear relationship between the (0002) peak positions and the alloy composition imply that the unit cell continuously expands in the c-direction from $ZnGeN_2$ to $ZnSnN_2$, which is consistent with experimental data for the unit cell of the end materials. $ZnGeN_2$ has been shown to have a c-lattice constant 0.515 nm by Narang *et al.* [4], whereas $ZnSnN_2$ has a c-lattice constant 0.554 nm as reported by Olsen *et al.* [2].

To make a comparison between $ZnSn_xGe_{1-x}N_2$ and the $In_xGa_{1-x}N$ alloys, it is worth noting that $ZnSn_xGe_{1-x}N_2$ exhibits a compositional uniformity that differs from the behavior of the $In_xGa_{1-x}N$ alloys. The large lattice mismatch between InN and GaN causes segregation and phase separations in alloys with a high indium content. This behavior is in contrast to the observed compositional uniformity in $ZnSn_xGe_{1-x}N_2$. In terms of x-ray diffraction measurements, phase-separated $In_xGa_{1-x}N$ typically displays two separate peaks, representing the two different lattice parameters present in the material [4].

For further examinations of the crystallograpic properties, ϕ-scans were also performed throughout the alloy. Investigating the rotational symmetry of the asymmetrical (101)-plane in both $ZnSn_xGe_{1-x}N_2$ and ZnO. Figure 4.7 display ϕ-scans of the alloys, where six distinct reflection peaks separated with 60°, confirm the sixfold symmetry of the hexagonal wurtzite crystal in both the thin film and the substrate. The six $ZnSn_xGe_{1-x}N_2$ (101) reflections

also overlap perfectly with the corresponding ZnO peaks, indicating no rotation of the thin film unit cell to reduce the lattice mismatch, as is common for e.g., ZnO grown on c-Al_2O_3, [44].

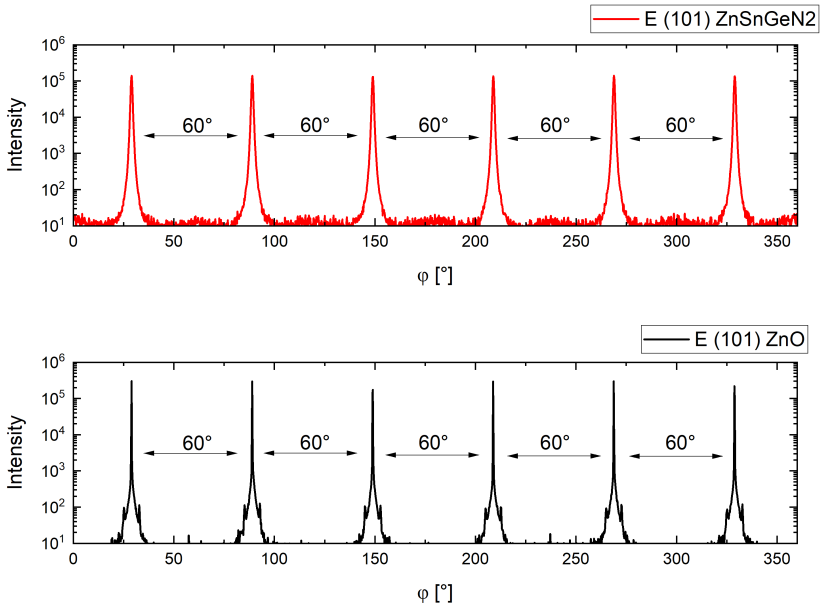

Figure 4.7: Phi-scans of sample E, where the (101) ZnO plane is showed in black and (101) $ZnSnGeN_2$ plane is showed in red.

4.4.2 Optical Properties

The alloys optical properties have been examined through UV-Vis and FTIR, carried out with transmission and reflection measurements. Raw data from a transmission scan is presented in figure 4.8a, showing the percentage of light transmitted through the stoichiometric $ZnSn_xGe_{1-x}N_2$ alloy series, as a function of the wavelength of the incident light. Considering the inverse proportionality between wavelength and frequency, it is worth remembering that shorter wavelengths carry more energy than longer ones. Within the range of high-energy electromagnetic waves, with wavelengths of approximately less than 400 nm, the absence of transmitted light indicates that the thin films either reflect or absorb the full amount of the incident light. In this spectral region the excess energy of the photons is sufficient to excite electrons over the bandgaps. A reduction in transmission can be seen in the area $500 < \lambda < 1000$ nm for all the stoichiometric alloys in figure 4.8. The drop shifts as a function of alloy composition, indicating that the samples interact differently with the incident light, due to different bandgaps sizes. The incorporation of Sn in the alloys, with the exception of $ZnSnN_2$, experience a red shift in the transmission onset over the visible spectrum. This behavior is related to a shift in absorption, and gives an indication that the bandgap energies are smaller for Sn-rich alloys compared to Ge-rich alloys.

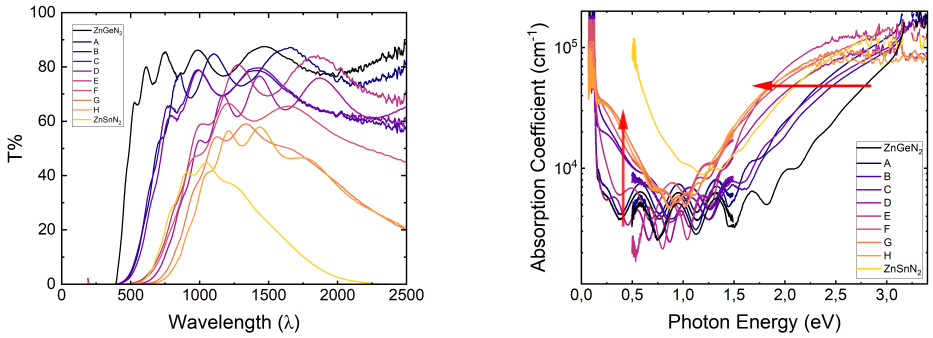

(a) (b)

Figure 4.8: (a) Transmission spectrum measured with UV-Vis. (b) Calculated absorption coefficient, α, including transmission and reflection data from both UV-Vis and FTIR measurements.

The wavy shape of the transmission in the IR region ($1000 < \lambda < 2500$ nm) is due to interference caused by the thickness and is an indication of a flat surface and uniform film thickness. The transmission for the various alloys is showing a clear reduction with increased Sn-content at extended wavelengths of the electromagnetic spectrum. For the Ge-rich samples there is close to no absorption below the bandgap of the alloy. On the other hand, there is a strong absorption for photon energies well below the bandgap for the more Sn-rich samples, and especially pure $ZnSnN_2$. This absorption may be due to the presence of free carriers in the Sn-rich samples. Free carrier absorption is a phenomenon that occurs when a material absorbs a photon, and a carrier is exited from an already exited state to another unoccupied state in the same band.

To further investigate the optical properties, the absorption coefficient α from both UV-Vis and FTIR measurements are plotted as a function of photon energy in figure 4.8b. The absorption coefficients close to the absorption onset ($\sim$ 1.5 eV - $\sim$ 2.5 eV) provides the same tendency with a red shift through the alloys as the Sn composition increases, with the exception of $ZnSnN_2$. The absorption coefficients provided by FTIR shows a trend at lower energies ($\sim$ 0 eV - $\sim$ 0.5 eV), indicating an increase in the absorption coefficient for Sn-rich samples, supporting the theory of presence of free carrier absorption. This trend in increased amount of free carriers for Sn-rich samples could be linked to the increasing carrier concentration for Sn-rich alloys. Additionally, $ZnSnN_2$ shows a clear increase in absorption coefficient for energies higher than that of the rest of the alloys. Interestingly, $ZnSnN_2$ deviates from both trends. It is important to note that the incident light interacts with both the thin films and substrates during UV-Vis and FTIR measurments. Even though ZnO is a transparent material, both components will contribute and may introduce a source of error. The influence of ZnO can also result in relatively large uncertainties in the estimated bandgaps when using transmittance and reflection measurements.

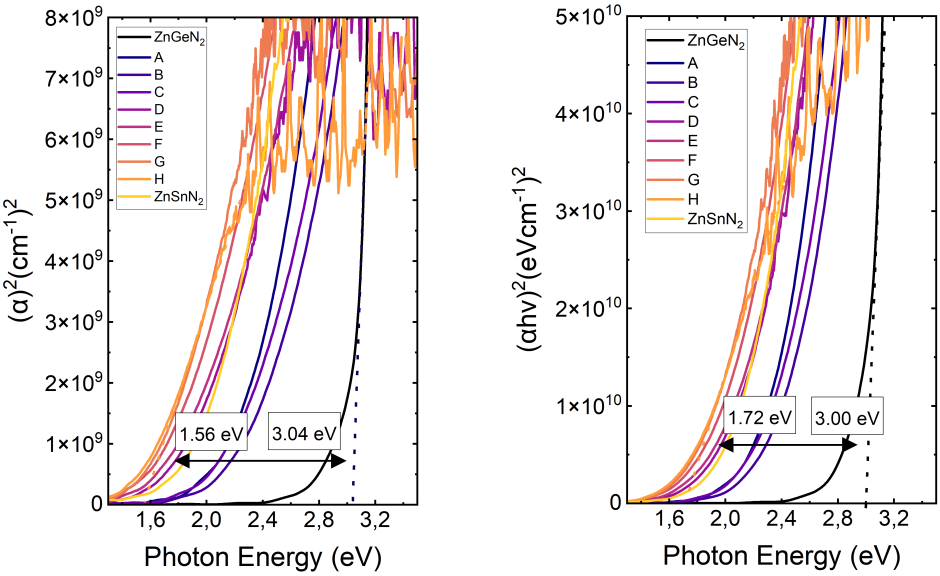

(a) (b)

Figure 4.9: The optical bandgaps of the stoichiometric alloys were estimated by (a) α^2 plot, resulting in a range of 1.56 eV to 2.34 eV and (b) Tauc plot varying from 1.72 eV to 2.37 eV. In both cases, the optical bandgaps were estimated by performing a linear extrapolation and identifying the intersection of the resulting line with the energy axis.

The size of the optical bandgaps have been estimated by the use of two different methods. Since the alloys are direct bandgap semiconductors, taking the linear extrapolation of the linear region of a plot consisting of α^2 versus the photon energy is one of them [41]. By doing so, showed in figure 4.9a, an estimate of the bandgaps through the alloy is ranging from 1.56 eV to 3.04 eV. Tauc plots are another well-established estimation method for optical bandgaps [41]. Here, and as shown in figure 4.9b, the Tauc analysis result in bandgap estimates in a range from 1.72 eV to 3.00 eV. In figure 4.10 the change in optical bandgap is plotted as a function of alloy composition.

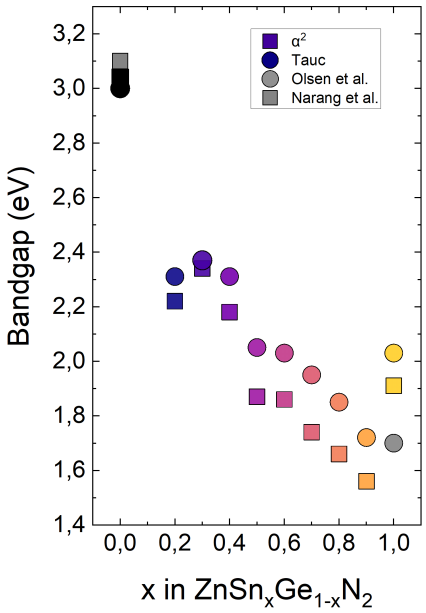

Figure 4.10: Bandgap estimations for the $ZnSn_xGe_{1-x}N_2$ alloys with varying compositions. Squares indicates the Tauc method and circles are calculated with α^2.

Figure 4.10 shows a tunable bandgap of the stoichiometric alloy series by changing the Sn/Ge ratio. According to Coronel *et al.* [45], $ZnSn_xGe_{1-x}N_2$ alloys made by reactive RF sputtering have bandgaps between 1.8 – 3.1 eV, which is in good agreement with the results obtained in this work. The estimated bandgap of pure $ZnGeN_2$ is consistent with the research done by Narang *et al.* [4], with a size of approximately 3.0 - 3.1 eV (see figure 4.10). The bandgap trend for the $ZnSn_xGe_{1-x}N_2$ alloys exhibits a gap between sample A (with $x = 20$) and $ZnGeN_2$, which could not be covered due to unstable growth for the Ge-rich thin films. While the rest of the alloys show a nearly linear relationship between alloy composition and bandgap (figure 4.10). However, $ZnSnN_2$ shows an increased bandgap estimation compared to the other alloys, deviating from this trend. Olsen [2], was able to grow high-quality $ZnSnN_2$, estimated a bandgap value of approximately 1.7 eV. This shows good consensus with the trend of the Sn-rich alloys, but was not achieved for the $ZnSnN_2$ sample. For a $ZnSn_xGe_{1-x}N_2$ alloy to work with Si in a tandem solar cell, the area of lower bandgap values, approximately 1.7 eV, is of most interest. Fioretti *et al.* [7] showed that bandgap tuning could be achieved over an even wider energy range by varying growth or annealing temperature to control disorder for $ZnSnN_2$.

4.4.3 Electrical Properties

Room temperature and temperature dependent Hall effect measurements were conducted using van der Pauw configuration and with a magnetic field strength of 10 kG, where specific information like the thickness and length was taken into account. Figure 4.11 presents the carrier density and mobility, extracted from Hall effect measurements, as a function of alloy composition at room temperature. The alloys carrier concentration, presented

in Figure 4.11a, shows a clear reduction in concentration, tuning the alloy from $ZnSnN_2$ to $ZnGeN_2$. $ZnSnN_2$ have a concentration as high as 7.38×10^{20} cm^{-3}. By exchanging Sn with Ge the alloy exhibit a nearly linear decrease in carrier concentration, with the exception of sample B ($x = 30$), as the only one deviating from this trend. The carrier density is similar for the most Ge-rich sample, A, and $ZnGeN_2$ at 1.51×10^{18} cm^{-3} and 1.62×10^{18} cm^{-3}, respectively. Nonetheless, the linear decrease in carrier concentration through the alloy indicates a possibility of tuning the carrier concentration by changing the content of the four-valence cations, Sn and Ge. Shing *et al.* [6] successfully sputtered several $ZnSn_xGe_{1-x}N_2$ alloys in the Ge-rich region, where the carrier concentrations were measured as low as $\sim 10^{11}$ cm^{-3} for alloys with less than 5% Sn, and reached a plateau at $\sim 10^{21}$ cm^{-3} at 15% Sn atomic level. It is also important to note that the high carrier concentration for the Sn-rich samples might affect the bandgap estimations in Figure 4.10 due to the Burstein-Moss shift [46, 47]. The Moss-Burstein effect is a phenomenon observed in some degenerate semiconductors when the doping concentration is so high that some states in the conduction band become populated, leading to a falsely high bandgap estimate. This effect could also be present in alloys exhibiting the highest concentration of charge carriers, such as $ZnSnN_2$.

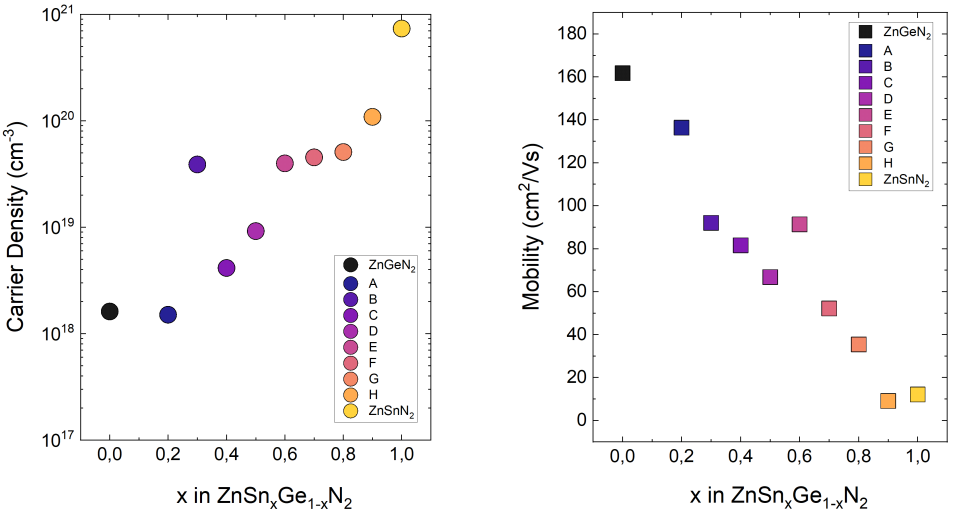

(a) (b)

Figure 4.11: (a) Carrier concentration and (b) mobility for the stoichiometric alloy series measured at room temperature.

The mobility, seen in figure 4.11b, is closely related to the carrier concentration and decreases close to linearly with the Sn-concentration. $ZnGeN_2$ yields a mobility as high as 161.7 cm^2/Vs, decreasing down to sample H and $ZnSnN_2$, with mobilities of 9.1 cm^2/Vs and 12.1 cm^2/Vs, respectively. In comparison, Shing *et al.* [6] only achieved mobilites under 10 cm^2/Vs for the entire alloy, and with an average mobility of $\sim$2 cm^2/Vs. On the other hand, Gogova *et al.* [19] measured mobility of 38 cm^2/Vs in high quality $ZnSnN_2$, suggesting that the mobility in our samples may be lower due to the slightly lower crystal quality. The

mobilities achieved here are substantially improved for the majority of the thin films, where several of the alloys have mobilities over ∼50 cm^2/Vs, which is typically the lower limit of the mobility range for materials used in a pn-junction and solar applications.

Phonon scattering and impurity scattering are the two main mechanisms that impact the mobility of charge carriers in a material. Phonon scattering occurs when vibrations in the atomic lattice interact with the moving charge carriers. This mechanism typically dominates at higher temperatures, as the lattice vibrations increase with temperature, leading to a decrease in mobility with a temperature dependency of approximately $T^{-3/2}$ [11]. On the other hand, impurity scattering cause a decrease in mobility with decreasing temperature. Since the charge carriers have less velocity at lower temperatures, they are also more likely to be scattered by collisions with impurities in the material. This mechanism dominates at lower temperatures, with a temperature dependency of approximately $T^{3/2}$ [11]. According to Hamilton *et al.* [48] is the dominating limitation scattering effect on $ZnSnN_2$ at room temperature caused by neutral impurities.

Temperature dependent Hall measurements is shown in figure 4.12 in a range of $20 - 300$ K. For the mobility, figure 4.12b, it is a clear indication that the most Ge-rich samples, containing highest mobility at room temperature, are the ones exhibiting most variations due to the changes in temperature. Sample A can be seen to exhibit a maximum mobility of > 400 cm^2/Vs in the temperature range of $90 - 100$ K. The most Sn-rich samples exhibits smaller variations in the mobility as a function of temperature. Figure 4.12a presents the carrier concentration of the various thin films as a function of temperature. The figure reveal that the carrier density of the majority of the stoichiometric alloys are affected, and in general decrease with decreasing temperature. Normally, semiconducturs are more conductive at higher temperatures, due to the fact that more electrons are thermally excited to the conduction band at higher temperatures. It is therefore interesting to note that the carrier density of several of the stoichiometric thin films again increases at even lower temperatures. One possible explanation for this feature is the formation of a degenerate interface layer between the substrate and the thin film bulk. This has been observed for GaN growth, and yields an increace in carrier concentrations at lower temperatures [49].

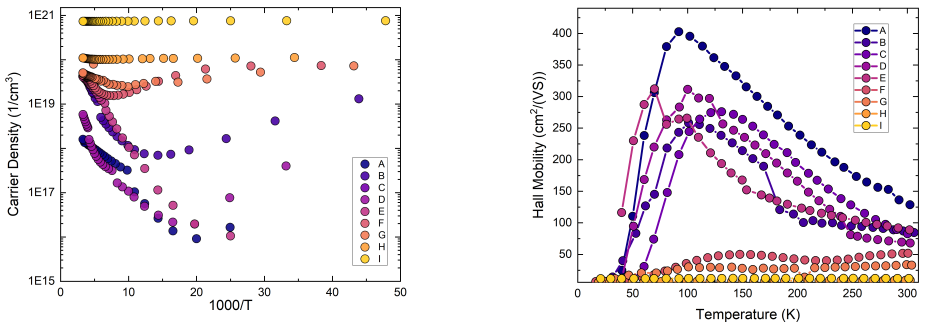

(a) (b)

Figure 4.12: (a) Carrier concentration and (b) mobility at varied temperatures.

In summary, the stoichiometric $ZnSn_xGe_{1-x}N_2$ alloys posses good quality thin films with a hexagonal symmetry and a primary growth direction in the (0002), similar to that of the ZnO substrate. However, the observation of additional diffraction peaks indicate the presence of different phases within the alloys. The continuous shift in the (0002) diffracting angle throughout the alloy, as a function of composition, suggests an alloy with a continuous expansion of c-lattice constant from $ZnGeN_2$ to $ZnSnN_2$. The estimated optical bandgaps of the stoichiometric alloys range from 1.56 eV to 3.04 eV, demonstrating a linear tunability dependent on the alloy composition. For electrical properties, the carrier density and mobility exhibits almost linear behavior with respect to the alloy composition. $ZnSnN_2$ exhibits a carrier concentration of 7.38×10^{20} cm^{-3} and $ZnGeN_2$ exhibits a carrier concentration of 1.62×10^{18} cm^{-3}, and where the alloys exchanging Sn/Ge ratio, exhibited carrier densities in between these to values. The mobility ranges from 161.7 cm^2/Vs for $ZnGeN_2$ to 12.1 cm^2/Vs for $ZnSnN_2$.

4.5 Non-stoichimetric $ZnSn_xGe_{1-x}N_2$ Alloy

A series of non-stoichiometric $ZnSn_xGe_{1-x}N_2$ alloys were investigated as an approach to reduce the high carrier concentrations found in the stoichiometric series in the Sn-rich region. As demonstrated by Fioretti *et al.* [7], the growth of non-stoichiometric, Zn-rich, $ZnSnN_2$ gives a higher probability of crating Zn_{Sn} antisites (acceptors) as opposed to Sn_{Zn} donors, and thereby reduce the carrier concentration. Building upon this knowledge, the present study explore the potential for achieving similar outcomes by growing the entire $ZnSn_xGe_{1-x}N_2$ alloy series in a non-stoichiometric manner, something that has not been reported before. The non-stoichiometric alloy was grown on P-implanted ZnO and labeled A2-I2. Where A2 is the most Ge-rich sample with $x = 0.17$ and I2 is $ZnSnN_2$. Non-stochiometric $ZnGeN_2$ was not attempted in this work, as the stoichiometric compound already display reasonable charge carrier concentration. The cation ratio of the non-stoichiometric alloys were increased from ≈ 0.50 in the stoichiometric alloys, to Zn/(Zn+Sn+Ge) $\approx 0.55 - 0.60$, while the alloy compositions were attempted to match the stoichiometric thin films. Fioretti *et al.* [7] alleged that a cation stoichiometry between $0.6 - 0.65$ was necessary to observe a significant reduction, but due to difficulties with incorporating enough Zn into the thin films, an alloy series with lower cation stoichiometry was investigated. The composition of the non-stoichiometric samples is presented in table 4.5.

Table 4.5: Composition of the non-stoichiometric alloy samples. The cation stoichiometry and alloy composition are extracted with SEM EDS, while the thickness was obtained by stylus profilometer measurements.

Non-Stoichiometric Alloy Samples			
Sample name	Cation stoichiometry II/II+IV	Alloy composition Sn_xGe_{1-x}	Thickness [nm]
A2	0.56	0.17	710.0
B2	0.55	0.31	676.1
C2	0.51	0.36	607.4
D2	0.63	0.53	1258.3
E2	0.59	0.58	660.0
G2	0.62	0.76	1055.2
H2	0.59	0.84	1056.1
I2 ($ZnSnN_2$)	0.54	1.00	999.4

4.5.1 Structural Properties

The crystal structure of the non-stoichiometric samples were examined with the same XRD instrumentation as the stoichiometric samples, making them easily comparable. Figure 4.13 shows $2\theta - \omega$ scans of the non-stoichiometric alloy with the diffraction intensity plotted as a function of the diffracting angle. As for the stoichiometric alloy, the non-stoichiometric alloy shows diffraction of the (0002) ZnO and (0002) $ZnSnGeN_2$, in addition to the (0004) reflections of the two planes. Less intense peaks are, as for the stoichiometric alloy, also present at ∼13.8° and ∼53°, marked by dotted lines. The peak at the lowest diffracting angle is only occurring for sample G, making it challenging to identify. The peak at ∼53° are shown in both Sn-rich and Ge-rich samples, and could potentially be the (440) plane of Zn_3N_2. On the other hand, the fact that this peak is less intense for the Zn-rich samples compared to the stoichiometric samples displayed in Figure 4.5, makes this peak challenging to identify. Something that distinguishes the wide $2\theta - \omega$ scan of the non-stoichiometric alloy from the stoichiometric is the diffraction peak observed shifting from ∼49.22° in sample H2 to ∼51.73 in sample A2. The peak seems to vary depending on the alloy, shifting to a higher angle with increased Ge-content, indicating that the peak is thin-film related. Without being a perfect match, possible candidates for this diffraction peak are the alloys (110) $ZnGeN_2$ at 57°, (102) $ZnGeN_2$ at 48° and (110) $ZnSnN_2$ at 54°. Where the (100) and (102) $ZnGeN_2$ is sourced from ICDD (International centre for diffraction data) database, which don't have information about $ZnSnN_2$. Due to the observed shift for the peak, it could be a thin film-related peak originating from a combination of these planes. In that case, the non-stoichiometric samples are polycrystalline.

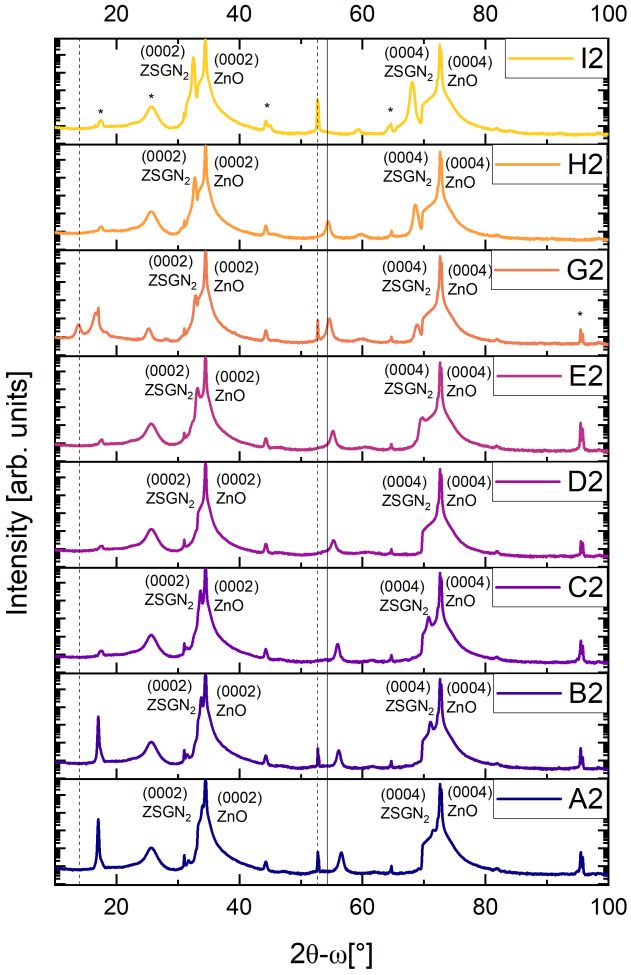

Figure 4.13: Wide $2\theta - \omega$ scan of the non-stoichiometric alloys.

Figure 4.14a shows a $2\theta - \omega$ scan, highlighting the diffraction of the (0002) planes. The absence of a $ZnSnGeN_2$ (0002) peak in sample D indicates that there is no growth in the <0001> direction. Likewise, the minor diffraction observed in sample G suggests that this growth direction is not favored in these alloys when grown non-stoichiometric. The remaining alloys show distinct (0002) alloy peak in addition to the (0002) ZnO peak. The thin films exhibit only one distinct (0002) peak, and a linear shift between the two end materials suggests that $ZnSn_xGe_{1-x}N_2$ is an alloy with a variable composition, and do not consist of several phases. Even though the alloy is not very non-stoichiometric, the intensities are greatly diminished compared to the stoichiometric alloys, indicating a lower crystal quality, with the exception of sample I2 ($ZnSnN_2$), as the only one having an intensity in the range of the stoichiometric samples. This is probably because the level of non-stoichiometry is very low.

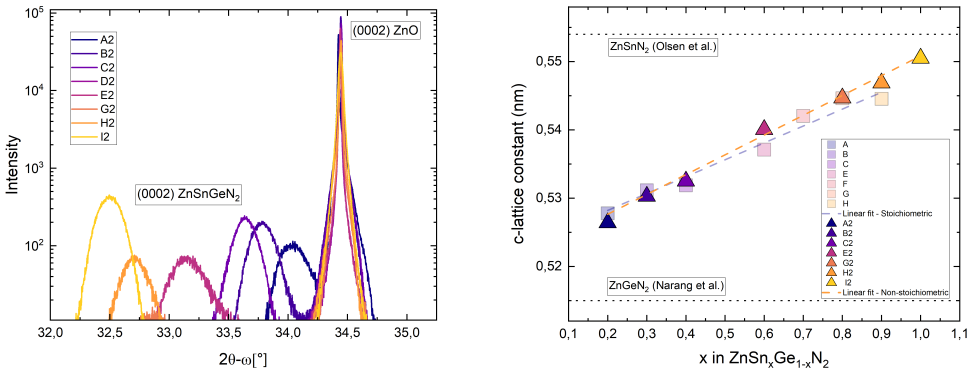

(a) (b)

Figure 4.14: (a) shows $2\theta - \omega$ scans emphasizing the (0002) diffraction of the non-stoichiometric alloy series. (b) presents the calculated c-lattice constants, where the triangles shows the non-stoichiometric samples, and the faded squares presents the stoichiometric samples for comparison, with a linear fit for both the alloy series.

The $2\theta - \omega$ peak positions of the (0002) alloy diffraction is used to plot the c-lattice constant as a function of alloy composition in figure 4.14b. The triangles presents a close to linear trend in the expansion of the lattice constant moving from $ZnGeN_2$ to $ZnSnN_2$ of the non-stoichiometric series. For comparison, the faded squares shows the stoichiometric alloys, indicating a tendency of slightly smaller lattice constant in the Sn-rich part, otherwise, their appearance exhibits a high degree of similarity. Note that there is a change in the lattice constants between the stoichiometric and non-stoichiometric alloy series, especially for the more Sn-rich samples. A possible explanation for the decrease in crystal structure can be strain, even though this do not fully explain the decrease in quality for the Ge-rich samples.

4.5.2 Optical Properties

The optical bandgaps were estimated using α^2- and Tauc-plots, see figure 4.15, yielding values ranging from 1.56 eV to 2.19 eV and 1.71 eV to 2.24 eV, respectively. By altering the Sn/Ge ratio, the non-stoichiometric alloy series displays a tunable bandgap, closely resembling the stoichiometric series. In figure 4.16 the change in optical bandgap is plotted as a function of composition, revealing that the non-stoichiometric samples have slightly lower bandgap estimates, but follow the same trend as the stoichiometric alloy series. One can therefore argue that the light interacts quite similarly for the non-stoichiometric samples as the stoichiometric ones.

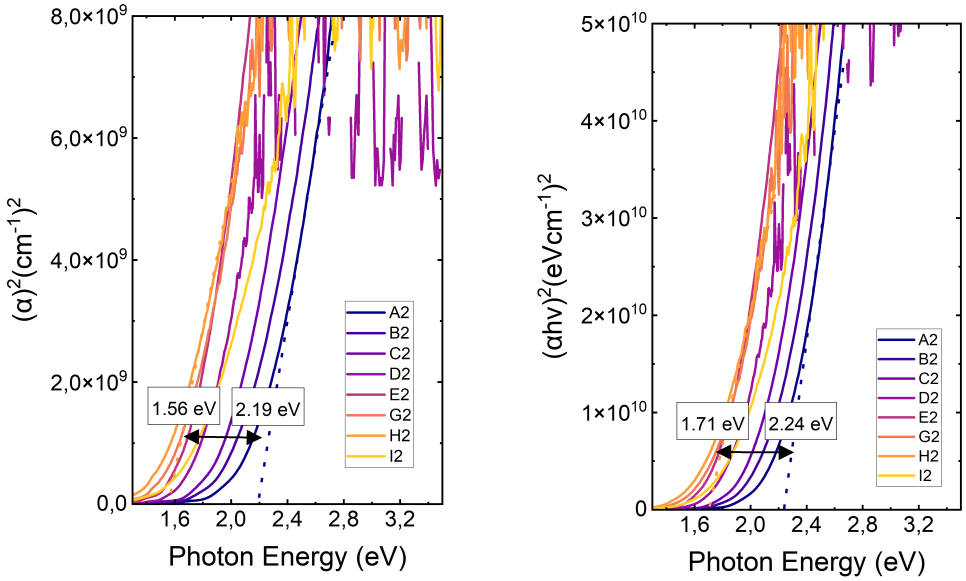

(a) (b)

Figure 4.15: The size of the optical bandgap for the non-stoichiometric alloy were estimated by (a) α^2 plot, resulting in a range of 1.56 eV to 2.19 eV and (b) Tauc plot varying from 1.71 eV to 2.24 eV. In both cases, the optical bandgaps were estimated by performing a linear extrapolation and identifying the intersection of the resulting line with the energy axis.

The non-stoichiometric alloys exhibit a consistent reduction in bandgap compared to the stoichiometric alloy, with the effect being particularly pronounced in thin films located closer to the center of the alloy. Cation disorder is known to have an impact on the optical bandgap [7], and could be a factor in the reduced bandgap for the non-stoichiometric alloys. Another possibility for the reduction of bandgap is a Burstein Moss shift, which could reduce the optical bandgaps in the non-stoichiometric alloy due to lower carrier concentration. However, this is not in full agreement with the electrical properties, as the bandgap is reduced for all the alloys, and not only the ones exhibiting charge carriers in the degenerated level for the stoichiometric films. This does not exclude that Burstin-Moss shifts are happening, but it is not likely to be the only reason for the drop in bandgap between the stoichiometric and non-stoichiometric.

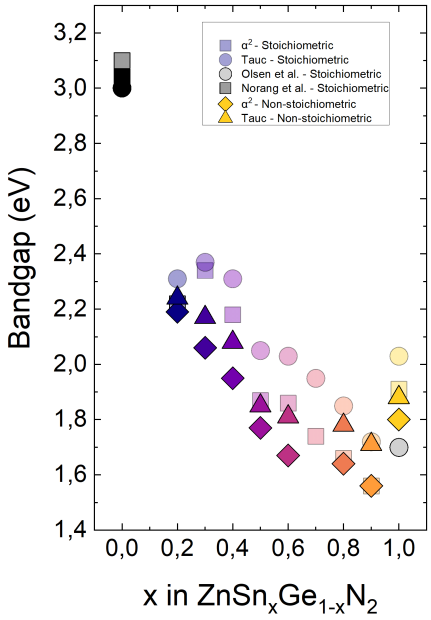

Figure 4.16: Bandgap estimations for the non-stoichiometric $ZnSn_xGe_{1-x}N_2$ alloys with varying compositions. Triangles indicates the Tauc method and rotated squares are calculated with α^2. The bandgap estimations of the stoichiometric alloy is showed in faded colors for comparison.

4.5.3 Electrical Properties

The aim of growing an additional non-stoichiometric alloy series was to potentially achieve further reduction of the concentration of charge carriers, as obtained by Fioretti [7] for $ZnSnN_2$. By the use of Hall measurements the electrical properties were examined, where the carrier density and mobility at room temperature is shown in figure 4.17. The carrier density of the non-stoichiometric samples are presented by triangles, while the stoichiometric samples are included as faded circles, see figure 4.17a. The trend through the alloy compositions for the non-stoichiometric alloys is not as linear as the stoichiometric alloy, but shows a clear tunability of the carrier density. Non-stoichiometric $ZnSnN_2$ exhibits a charge density as high as 10^{21} cm^{-3}, which is only slightly lower than that of stoichiometric $ZnSnN_2$, and in contrast to that reported by Fioretti *et al.* [7]. Note, however, that the non-stoichiometric alloys have a cation-stoichiometry of approximently $0.5 - 0.6$, which is lower than Fioretti used [7]. Therefore, there is a high possibility that the samples are not sufficiently non-stoichiometric to achieve a real drop in carrier density. On the other hand, for the majority of the alloys there is a tendency of reduced carrier density, indicating that a reduction of Sn_{Zn} compared to Zn_{Sn} antisites have been achieved, although possibly not to it's full potential.

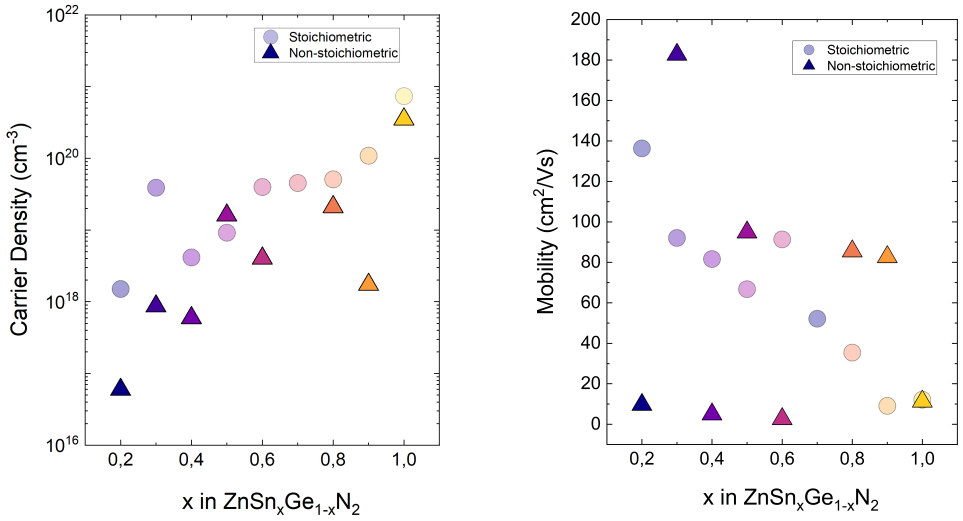

(a) (b)

Figure 4.17: (a) Carrier concentration and (b) mobility for the non-stoichiometric alloy series measured at room temperature.

The mobilities of the non-stoichiometric samples do not display a clear trend, in contrast to the ones of the stoichiometric alloy, see figure 4.17b. It is notable that the mobility of sample A, C, E and $ZnSnN_2$ have very low mobilities, > 15 cm^2/Vs, compared to the rest of the non-stoichiometric alloys. Nevertheless, A, C and E are in good agreement with the mobility Shing *et al.* [6] achieved for a stoichiometric $ZnSn_xGe_{1-x}N_2$ alloy series, showing no correlation between the composition and the mobility. The rest of the non-stoichiometric alloys can indicate an compositional dependency, where the mobility of the alloy decrease with reducing Ge concentration relative to Sn, as observed in the stoichiometric alloy.

Temperature dependent Hall measurements were conducted on the non-stoichiometric alloy series, although some of the samples could not be measured at very low temperatures. Figure 4.18 displays the carrier density and mobility as a function of temperature. As shown in Figure 4.18a, the carrier density of $ZnSnN_2$ does not exhibit a clear dependence on temperature for either stoichiometric and non-stoichiometric alloys. Only sample H2 among the non-stoichiometric alloys shows a trend of reduced carrier concentration at low temperatures, followed by an increase at even lower temperatures. This phenomenon was also observed in the stoichiometric alloys, which may indicate the presence of degenerate states. However, this is unlikely for H2, which has a carrier density of approximately 10^{18} cm^{-3}. Sample B2 and G2 exhibit a near-linear reduction in concentration as a function of temperature. Figure 4.18b presents the mobility measures from 20 K up to room temperature, where sample B stands out with a mobility as high as > 700 cm^2/Vs at approximately 60 K.

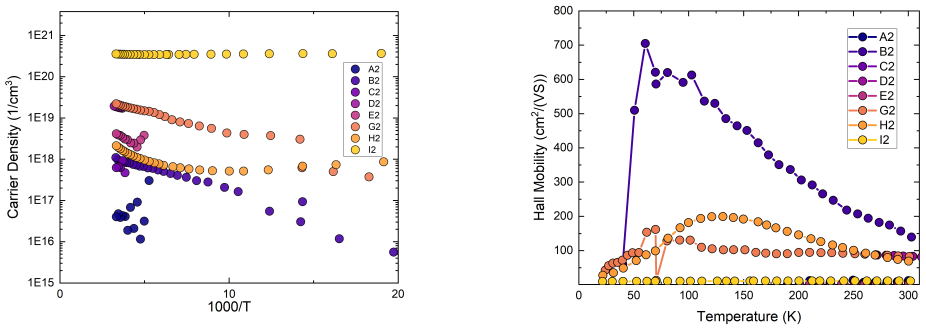

(a) (b)

Figure 4.18: (a) Carrier concentration and (b) mobility at varied temperatures.

To summarize, a non-stoichiometric alloy with a near-full compositional range was grown, having a cation ratio Zn/(Zn+Sn+Ge) $\approx 0.55 - 0.6$. The resulting thin films exhibited lower crystal quality than the stoichiometric alloy, as indicated by lower intensity (0002) diffraction peaks. However, the non-stoichiometric alloy exhibited shifts in it's wurtzite (0002) alloy peaks position and c-lattice constant, revealing that it was actually a random alloy and not simply a combination of $ZnGeN_2$ and $ZnSnN_2$ phases. The detection of Bragg diffraction patterns that are most likely related to the alloy suggests the presence of other phases or compounds in the films. The optical bandgap of the non-stoichiometric alloy was found to be tunable, ranging from 1.56 eV to 2.24 eV depending on the alloy composition. Additionally, the carrier density of the non-stoichiometric alloy was tunable from approximately 10^{21} cm^{-3} to 10^{17} cm^{-3}, while the mobilities exhibited only small tendencies toward a trend, covering mobilities as high as > 180 cm^2/Vs, and as low as < 10 cm^2/Vs.

Chapter 5

Conclusion

This experimental study investigated the novel alloy $ZnSn_xGe_{1-x}N_2$, including both stoichiometric and non-stoichiometric alloy series with a nearly full compositional range of $0 \leq x \leq 1$. The study aimed to gain a better understanding and control of the structure, optical, and electrical properties of the material for potential use in tandem solar cells.

The results demonstrate the successful fabrication of high quality $ZnSn_xGe_{1-x}N_2$ alloys, with the ability to tune both carrier concentration and the optical bandgap as a function of composition. Stoichiometric $ZnSn_xGe_{1-x}N_2$ alloys exhibited good quality, but also showed the presence of different phases within the alloys, yielding an alloy with a (0002) preferred orientation. The continuous shift in the (0002) diffracting angle throughout the alloy suggests an alloy with a continuous expansion of c-lattice constant from $ZnGeN_2$ to $ZnSnN_2$. The estimated optical bandgaps of the stoichiometric alloy range from 1.56 eV to 3.04 eV, demonstrating linear tunability depending on the alloy composition. For electrical properties, the carrier density and mobility exhibited almost linear behavior with respect to the alloy composition. The mobility ranges from 161.7 cm^2/Vs for $ZnGeN_2$ to 12.1 cm^2/Vs for $ZnSnN_2$. Shifting the alloy composition, the carrier concentration is reduced from 7.38×10^{20} cm^{-3} for $ZnSnN_2$ to 1.62×10^{18} cm^{-3} for $ZnGeN_2$. However, the high carrier concentration could cause a Burstein-Moss shift, where the high number of carriers in the conduction band causes degenerate states, affecting the estimated E_g values.

In addition, a non-stoichiometric alloy with a near-full compositional range was grown, with a cation ratio $Zn/(Zn+Sn+Ge) \approx 0.55 - 0.6$. The resulting thin films exhibited lower crystal quality than the stoichiometric alloy, and a more polycrystalline nature. The non-stoichiometric alloy exhibited shifts in it's wurtzite (0002) alloy peaks and c-lattice constant, revealing that it was actually a random alloy and not simply a combination of $ZnGeN_2$ and $ZnSnN_2$ phases. However, the detection of additional Bragg diffraction peaks that are most likely related to the alloy suggests the presence of other phases or compounds in the films. The optical bandgap of the non-stoichiometric alloy was found to be tunable, but with a slightly lower value than the stoichiometric, ranging from 1.56 eV to 2.24 eV depending on the alloy composition. Additionally, the carrier density of the non-stoichiometric alloy was tunable from approximately 10^{21} cm^{-3} to 10^{17} cm^{-3}, while the mobilities exhibited only

small tendencies toward a trend, covering mobilities as high as > 180 cm^2/Vs, and as low as < 10 cm^2/Vs. It is most likely due to insufficient non-stoichiometry that the films do not achieve an even greater reduction in carrier concentration.

Overall, this study provides insights into the tunable properties of $ZnSn_xGe_{1-x}N_2$ alloys and their potential use in tandem solar cells. The successful growth of both stoichiometric and non-stoichiometric alloys with tunable optical and electrical properties could lead to further development of this material for solar cell applications.

5.1 Suggestions for future work

There is great potential for optimizing $ZnSn_xGe_{1-x}N_2$ for use in tandem solar cells, and this research has contributed to the understanding of the material, especially with the growth of a non-stoichiometric $ZnSn_xGe_{1-x}N_2$ alloys. However, there are several areas that could be explored in future work to further improve the material's properties.

In the current study, a considerable number of thin films with varying alloy compositions, including both stoichiometric and non-stoichiometric, were investigated. However, due to the large number of samples, the growth conditions were not individually tailored for each thin film. Future efforts could focus on optimizing the growth conditions for each sample, which would generate more reliable properties of the material and enhance the understanding of the alloy.

Another potential area of exploration is to increase the non-stoichiometry of the $ZnSn_xGe_{1-x}N_2$ alloy. Such an investigation would be interesting, as it could lead to lower carrier concentrations for the non-stoichiometric alloy series. In a previous study, Fioretti *et al.* [7] were able to achieve a higher level of non-stoichiometry, which could be pursued in future research on the $ZnSn_xGe_{1-x}N_2$ alloy.

Finally, it would be exciting to fabricate a diode using the $ZnSn_xGe_{1-x}N_2$ material to investigate it's potential for use in solar cell applications. This would provide valuable information on the material's electronic properties and could lead to for further research on the use of $ZnSn_xGe_{1-x}N_2$ in tandem solar cells.

Bibliography

[1] E. Raza and Z. Ahmad, "Review on two-terminal and four-terminal crystalline-silicon/perovskite tandem solar cells; progress, challenges, and future perspectives," *Energy Reports*, vol. 8, pp. 5820–5851, 2022.

[2] V. S. Olsen, V. Øversjøen, D. Gogova, B. Pécz, A. Galeckas, J. Borgersen, K. Karlsen, L. Vines, and A. Kuznetsov, "$ZnSnN_2$ in Real Space and k-Space: Lattice Constants, Dislocation Density, and Optical Band Gap," *Advanced Optical Materials*, vol. 9, no. 16, p. 2100015, 2021.

[3] F. H. Alharbi and S. Kais, "Theoretical limits of photovoltaics efficiency and possible improvements by intuitive approaches learned from photosynthesis and quantum coherence," *Renewable and Sustainable Energy Reviews*, vol. 43, pp. 1073–1089, 2015.

[4] P. Narang, S. Chen, N. C. Coronel, S. Gul, J. Yano, L.-W. Wang, N. S. Lewis, and H. A. Atwater, "Bandgap Tunability in $Zn(Sn,Ge)N_2$ semiconductor alloys," *Advanced Materials*, vol. 26, no. 8, pp. 1235–1241, 2014.

[5] A. M. Shing, N. C. Coronel, N. S. Lewis, and H. A. Atwater, "Semiconducting $ZnSn_xGe_{1-x}N_2$ alloys prepared by reactive radio-frequency sputtering," *APL Materials*, vol. 3, no. 7, p. 076104, 2015.

[6] A. Shing, Y. Tolstova, N. Lewis, and H. Atwater, "Growth of Epitaxial $ZnSn_xGe_{1-x}N_2$ Alloys by MBE," *Scientific Reports*, vol. 7, 09 2017.

[7] A. N. Fioretti, A. Zakutayev, H. Moutinho, C. Melamed, J. D. Perkins, A. G. Norman, M. Al-Jassim, E. S. Toberer, and A. C. Tamboli, "Combinatorial insights into doping control and transport properties of zinc tin nitride," *J. Mater. Chem. C*, vol. 3, pp. 11017–11028, 2015.

[8] C. Kittel, P. McEuen, and P. McEuen, *Introduction to solid state physics*, vol. 8. Wiley New York, 1996.

[9] R. J. Tilley, *Understanding solids: the science of materials*. John Wiley & Sons, 2004.

[10] J. A. Nelson, *The physics of solar cells*. World Scientific Publishing Company, 2003.

[11] B. G. Streetman, S. Banerjee, *et al.*, *Solid state electronic devices*, vol. 10. Pearson/Prentice Hall Upper Saddle River, 2006.

[12] J. Nord, K. Albe, P. Erhart, and K. Nordlund, "Modelling of compound semiconductors: analytical bond-order potential for gallium, nitrogen and gallium nitride," *Journal of Physics: Condensed Matter*, vol. 15, p. 5649, aug 2003.

[13] C. W. Leitz, M. T. Currie, M. L. Lee, Z.-Y. Cheng, D. A. Antoniadis, and E. A. Fitzgerald, "Hole mobility enhancements and alloy scattering-limited mobility in tensile strained Si/SiGe surface channel metal–oxide–semiconductor field-effect transistors," *Journal of Applied Physics*, vol. 92, pp. 3745–3751, 09 2002.

[14] E. Raza and Z. Ahmad, "Review on two-terminal and four-terminal crystalline-silicon/perovskite tandem solar cells; progress, challenges, and future perspectives," *Energy Reports*, vol. 8, pp. 5820–5851, 2022.

[15] P. VonDollen, S. Pimputkar, and J. S. Speck, "Let There Be Light—With Gallium Nitride: The 2014 Nobel Prize in Physics," *Angewandte Chemie International Edition*, vol. 53, no. 51, pp. 13978–13980, 2014.

[16] Y. Ye, R. Lim, and J. M. White, "High mobility amorphous zinc oxynitride semiconductor material for thin film transistors," *Journal of Applied Physics*, vol. 106, no. 7, p. 074512, 2009.

[17] J. Wu and W. Walukiewicz, "Band gaps of InN and group III nitride alloys," *Superlattices and Microstructures*, vol. 34, no. 1, pp. 63–75, 2003.

[18] I. S. Khan, K. N. Heinselman, and A. Zakutayev, "Review of $ZnSnN_2$ semiconductor material," *Journal of Physics: Energy*, vol. 2, p. 032007, jul 2020.

[19] D. Gogova, V. S. Olsen, C. Bazioti, I.-H. Lee, O. Prytz, L. Vines, and A. Y. Kuznetsov, "High electron mobility single-crystalline $ZnSnN_2$ on ZnO (0001) substrates," *CrystEngComm*, vol. 22, pp. 6268–6274, 2020.

[20] V. S. Olsen, Y. K. Frodason, Y. K. Hommedal, D. M. Nielsen, P. M. Weiser, K. M. H. Johansen, I.-H. Lee, A. Y. Kuznetsov, and L. Vines, "Li and group-III impurity doping in $ZnSnN_2$: Potential and limitations," *Phys. Rev. Mater.*, vol. 6, p. 124602, Dec 2022.

[21] S. Chen, P. Narang, H. A. Atwater, and L.-W. Wang, "Phase Stability and Defect Physics of a Ternary $ZnSnN_2$ Semiconductor: First Principles Insights," *Advanced Materials*, vol. 26, no. 2, pp. 311–315, 2014.

[22] C. L. Melamed, J. Pan, A. Mis, K. Heinselman, R. R. Schnepf, R. Woods-Robinson, J. J. Cordell, S. Lany, E. S. Toberer, and A. C. Tamboli, "Combinatorial investigation of structural and optical properties of cation-disordered $ZnGeN_2$," *J. Mater. Chem. C*, vol. 8, pp. 8736–8746, 2020.

[23] J. Breternitz and S. Schorr, "Symmetry relations in wurtzite nitrides and oxide nitrides and the curious case of $Pmc2_1$," *Acta Crystallographica Section A*, vol. 77, pp. 208–216, May 2021.

[24] E. W. Blanton, K. He, J. Shan, and K. Kash, "Characterization and control of $ZnGeN_2$ cation lattice ordering," *Journal of Crystal Growth*, vol. 461, pp. 38–45, 2017.

[25] J. J. Cordell, G. J. Tucker, A. Tamboli, and S. Lany, "Bandgap analysis and carrier localization in cation-disordered $ZnGeN_2$," *APL Materials*, vol. 10, no. 1, p. 011112, 2022.

[26] M. B. Tellekamp, C. L. Melamed, A. G. Norman, and A. Tamboli, "Heteroepitaxial Integration of $ZnGeN_2$ on GaN Buffers Using Molecular Beam Epitaxy," *Crystal Growth & Design*, vol. 20, no. 3, pp. 1868–1875, 2020.

[27] S. Limpijumnong, S. Rashkeev, and W. Lambrecht, "Electronic Structure and Optical Properties of $ZnGeN_2$," *MRS Internet Journal of Nitride Semiconductor Research*, vol. 4, pp. 600–605, 01 1999.

[28] W. R. L. Lambrecht and A. Punya, "519Heterovalent ternary II-IV-N_2 compounds: perspectives for a new class of wide-band-gap nitrides," in *III-Nitride Semiconductors and their Modern Devices*, Oxford University Press, 08 2013.

[29] J. Breternitz and S. Schorr, "Zinc germanium nitrides and oxide nitrides: the influence of oxygen on electronic and structural properties," *Faraday Discuss.*, vol. 239, pp. 219–234, 2022.

[30] N. Beddelem, S. Bruyère, F. Cleymand, S. Diliberto, C. Longeaud, S. le Gall, R. Templier, P. Miska, and B. Hyot, "Structural and functional properties of $Zn(Ge,Sn)N_2$ thin films deposited by reactive sputtering," *Thin Solid Films*, vol. 709, p. 138192, 2020.

[31] M. Taguchi, A. Yano, S. Tohoda, K. Matsuyama, Y. Nakamura, T. Nishiwaki, K. Fujita, and E. Maruyama, "24.7% record efficiency hit solar cell on thin silicon wafer," *IEEE Journal of Photovoltaics*, vol. 4, no. 1, pp. 96–99, 2014.

[32] K. Yoshikawa, W. Yoshida, T. Irie, H. Kawasaki, K. Konishi, H. Ishibashi, T. Asatani, D. Adachi, M. Kanematsu, H. Uzu, and K. Yamamoto, "Exceeding conversion efficiency of 26% by heterojunction interdigitated back contact solar cell with thin film Si technology," *Solar Energy Materials and Solar Cells*, vol. 173, pp. 37–42, 2017. Proceedings of the 7th international conference on Crystalline Silicon Photovoltaics.

[33] J. Werner, B. Niesen, and C. Ballif, "Perovskite/Silicon Tandem Solar Cells: Marriage of Convenience or True Love Story? – An Overview," *Advanced Materials Interfaces*, vol. 5, no. 1, p. 1700731, 2018.

[34] S. A. Campbell, *Fabrication engineering at the micro-and nanoscale.* No. Sirsi) i9780195320176, 2008.

[35] K. M. Krishnan, *Principles of Materials Characterization and Metrology.* Oxford University Press, 05 2021.

[36] Y. Leng, *Materials characterization: introduction to microscopic and spectroscopic methods*. John Wiley & Sons, 2009.

[37] V. S. Olsen, "Functional properties and band gap engineering of ZnO-GaN alloys," 2020.

[38] C. Bazioti, V. S. Olsen, A. Y. Kuznetsov, L. Vines, and Prytz, "Formation of N_2 bubbles along grain boundaries in $(ZnO)_{1-x}(GaN)_x$: nanoscale STEM-EELS studies," *Phys. Chem. Chem. Phys.*, vol. 22, pp. 3779–3783, 2020.

[39] F. Macheda, S. Poncé, F. Giustino, and N. Bonini, "Theory and Computation of Hall Scattering Factor in Graphene," *Nano Letters*, vol. 20, no. 12, pp. 8861–8865, 2020. PMID: 33226824.

[40] A. R. Zanatta and I. Chambouleyron, "Absorption edge, band tails, and disorder of amorphous semiconductors," *Phys. Rev. B*, vol. 53, pp. 3833–3836, Feb 1996.

[41] A. R. Zanatta, "Revisiting the optical bandgap of semiconductors and the proposal of a unified methodology to its determination," *Scientific reports*, vol. 9, no. 1, p. 11225, 2019.

[42] X.-M. Cai, B. Wang, F. Ye, J.-J. Zeng, K. Vaithinathan, F. Wang, X.-F. Ma, Y.-Z. Xie, D.-P. Zhang, P. Fan, and V. Roy, "Fabricating $ZnSnN_2$ with cosputtering," *Surface and Coatings Technology*, vol. 359, pp. 169–174, 2019.

[43] A. R. Denton and N. W. Ashcroft, "Vegard's law," *Phys. Rev. A*, vol. 43, pp. 3161–3164, Mar 1991.

[44] P. Fons, K. Iwata, S. Niki, A. Yamada, and K. Matsubara, "Growth of high-quality epitaxial ZnO films on α-Al_2O_3," *Journal of Crystal Growth*, vol. 201-202, pp. 627–632, 1999.

[45] N. C. Coronel, L. Lahourcade, K. T. Delaney, A. M. Shing, and H. A. Atwater, "Earth-abundant $ZnSn_xGe_{1-x}N_2$ alloys as potential photovoltaic absorber materials," in *2012 38th IEEE Photovoltaic Specialists Conference*, pp. 003204–003207, 2012.

[46] E. Burstein, "Anomalous Optical Absorption Limit in InSb," *Phys. Rev.*, vol. 93, pp. 632–633, Feb 1954.

[47] T. S. Moss, "The Interpretation of the Properties of Indium Antimonide," *Proceedings of the Physical Society. Section B*, vol. 67, p. 775, oct 1954.

[48] D. C. Hamilton, E. Arca, J. Pan, S. Siol, M. Young, S. Lany, and A. Zakutayev, "Electron scattering mechanisms in polycrystalline sputtered zinc tin oxynitride thin films," *Journal of Applied Physics*, vol. 126, 07 2019. 035701.

[49] D. C. Look and R. J. Molnar, "Degenerate layer at GaN/sapphire interface: Influence on Hall-effect measurements," *Applied Physics Letters*, vol. 70, pp. 3377–3379, 06 1997.